Repository of the Max Delbrück Center for Molecular Medicine (MDC) in the Helmholtz Association

https://edoc.mdc-berlin.de/16999

Adaptive and reversible resistance to Kras inhibition in pancreatic cancer cells

Chen P.Y., Muzumdar M.D., Dorans K.J., Robbins R., Bhutkar A., del Rosario A., Mertins P., Qiao J., Schafer A.C., Gertler F., Carr S. and Jacks T.

Adaptive and reversible resistance to Kras inhibition in pancreatic cancer cells

Pan-Yu Chen[a,b,g*], Mandar Deepak Muzumdar[a,c,d,h*], Kimberly Judith Dorans[a], Rebecca Robbins[a], Arjun Bhutkar[a], Amanda del Rosario[a], Philipp Mertins[e,i], Jana Qiao[e], Anette Claudia Schafer[a], Frank Gertler[a,b], Steven Carr[e] and Tyler Jacks[a,b,f,1]

[a] David H. Koch Institute for Integrative Cancer Research, Massachusetts Institute of Technology, 500 Main Street, Cambridge, MA 02139, USA
[b] Department of Biology, Massachusetts Institute of Technology, 77 Massachusetts Avenue, Cambridge, MA 02139, USA
[c] Harvard Medical School, 25 Shattuck Street, Boston, MA 02115, USA
[d] Dana-Farber Cancer Institute, 450 Brookline Avenue, Boston, MA 02115, USA
[e] Proteomics Platform, Broad Institute of MIT and Harvard, 415 Main Street, Cambridge, MA 02142, USA
[f] Howard Hughes Medical Institute, Massachusetts Institute of Technology, Cambridge, MA 02139, USA
[g] University of California, San Francisco, Helen Diller Family Cancer Research Building, 1450 Third Street, San Francisco, CA 94158, USA
[h] Department of Genetics, Yale University School of Medicine, 333 Cedar Street, New Haven, CT 06510, USA
[i] Proteomics Platform, Max Delbrück Center for Molecular Medicine in the Hemholtz Society and Berlin Institute of Health, 13125 Berlin, Germany
[*]These authors contributed equally to this work.
[1]To whom correspondence may be addressed. E-mail tjacks@mit.edu. Mailing address: 76-453, 500 Main Street, Cambridge, MA 02139, USA.

Running Title: Adaptive and reversible resistance to Kras inhibition

Key Words: Pancreatic cancer, cell adhesion, cell signaling, protein tyrosine kinases, animal models of cancer, gene expression profiling, oncogenes, tumor suppressor genes, gene products as targets for therapy, novel mechanisms

Conflict of Interest: The authors declare there are no conflict of interest.

1

ABSTRACT

Activating mutations in *KRAS* are the hallmark genetic alterations in pancreatic ductal adenocarcinoma (PDAC) and the key drivers of its initiation and progression. Longstanding efforts to develop novel KRAS inhibitors have been based on the assumption that PDAC cells are addicted to activated KRAS, but this assumption remains controversial. In this study, we analyzed the requirement of endogenous Kras to maintain survival of murine PDAC cells, using an inducible shRNA-based system that enables temporal control of Kras expression. We found that the majority of murine PDAC cells analyzed tolerated acute and sustained Kras silencing by adapting to a reversible cell state characterized by differences in cell morphology, proliferative kinetics, and tumor-initiating capacity. While we observed no significant mutational or transcriptional changes in the Kras-inhibited state, global phosphoproteomic profiling revealed significant alterations in cell signaling, including increased phosphorylation of focal adhesion pathway components. Accordingly, Kras-inhibited cells displayed prominent focal adhesion plaque structures, enhanced adherence properties, and increased dependency on adhesion for viability *in vitro*. Overall, our results call into question the degree to which PDAC cells are addicted to activated KRAS, by illustrating adaptive non-genetic and non-transcriptional mechanisms of resistance to Kras blockade. However, by identifying these mechanisms, our work also provides mechanistic directions to develop combination strategies that can help enforce the efficacy of KRAS inhibitors.

INTRODUCTION

Pancreatic cancer, of which 85% is pancreatic ductal adenocarcinoma (PDAC), is an aggressive disease that is largely refractory to frontline therapy (1). Although recent advances in multi-agent chemotherapy have increased median survival in advanced disease, the 5-year survival rate for PDAC patients remains low at 8% (2–4), making PDAC the third leading cause of cancer death in the United States (2) and underscoring an urgent need for novel therapies with improved efficacy and reduced toxicity.

Genomic studies revealed that *KRAS* mutations are the hallmark genetic feature of PDAC (5–7). *KRAS* encodes a GTPase that regulates diverse cellular processes, including proliferation and survival. In cancer cells, somatic missense mutations render KRAS insensitive to GTPase-activating proteins, resulting in the accumulation of GTP-bound KRAS and hyperactive effector signaling (8). As oncogenic KRAS signaling potentially contributes to multiple facets of malignant transformation, its precise biological functions in cancer appear context-dependent and remain to be fully elucidated (9–12).

The high frequency of activating *KRAS* mutations implies that oncogenic KRAS may drive PDAC initiation and progression. Mouse models have demonstrated that mutant *Kras* expression in the mouse pancreas leads to the development of precursor pancreatic intraepithelial neoplasia (PanINs) and PDAC, confirming the role of oncogenic Kras in tumor initiation (9,13,14). In contrast, the requirement of KRAS for PDAC maintenance remains unresolved. RNA interference-mediated knockdown of endogenous *KRAS* in human cell lines demonstrated variable dependency of PDAC cells on *KRAS* for survival (15). Accordingly, gene expression profiling of human PDAC tumors revealed distinct molecular subtypes associated with varying *KRAS* dependencies (16). In established *Kras*-driven mouse PDAC tumors, the withdrawal of

3

oncogenic *Kras* transgene expression resulted in rapid tumor regression, suggesting that sustained oncogenic *Kras* expression is essential for maintenance (9,11). Although the removal of oncogenic *Kras* is initially detrimental, tumor relapse via doxycycline-independent expression of the oncogenic *Kras* transgene and Kras-independent bypass mechanisms was observed (17,18).

Since at least a subset of PDAC cells and tumors exhibit *KRAS* oncogene addiction, KRAS inhibition is a compelling therapeutic approach. Unfortunately, effective pharmacological KRAS inhibitors have not yet been developed (8). A deeper understanding of the essentiality of KRAS for tumor maintenance and the degree of KRAS inhibition required to impair PDAC cell survival could provide insights into the role of KRAS in PDAC and facilitate the development of KRAS-directed therapies. Given that resistance against single-agent targeted therapies frequently emerges after prolonged treatment (19,20), it is critical to preemptively strategize treatment methods to circumvent resistance. Studies of cancer therapy resistance have led to the general conception that resistance often arises from the selection of pre-existing rare cells that have acquired resistance-conferring genetic alterations (20–22). In this case, combined inhibition of multiple nodes of a single pathway or simultaneous targeting of distinct pathways can be effective. However, recent studies have suggested that non-mutational mechanisms of drug resistance are also possible (19,20,23,24), for which intermittent dosing of the same inhibitor could induce a re-treatment response (25,26).

We assessed the requirement of oncogenic *KRAS* for PDAC maintenance and potential resistance mechanisms to KRAS inhibition by analyzing the consequence of acute and sustained Kras knockdown in murine PDAC cells *in vitro* and *in vivo*. Additionally, we conducted global gene expression and phosphoproteomic profiling of PDAC cells before and after *Kras*

4

knockdown to decipher mechanisms that mediate escape from *Kras* oncogene addiction.

Through these analyses, we defined an adaptive and reversible state of Kras inhibition marked by

prominent alterations in cell morphology, proliferative kinetics, and cell signaling. Importantly,

our work revealed candidate targets for rational combination therapies with novel KRAS

inhibitors in PDAC patients.

MATERIALS AND METHODS

Cell lines and culture conditions

A, B, and D parental cells were derived from three distinct primary pancreatic tumors from *; Pdx1-CreER*; *Kras$^{LSL-G12D/+}$; p53$^{flox/flox}$* mice treated with tamoxifen (Sigma) to induce oncogenic *Kras^{G12D}* activation and biallelic *p53* inactivation in the pancreas (13). Established human PDAC cell lines were obtained from the Broad Institute Cancer Cell Line Encyclopedia, sourced from DSMZ-Germany (8988T) American Type Culture Collection (ATCC) (PANC-1). Identity was authenticated by DNA fingerprinting by the Broad Institute. All cell lines were maintained in DMEM (Corning Cellgro) supplemented with 10% fetal bovine serum (Hyclone) and penicillin/streptomycin and tested negative for mycoplasma by PCR testing.

For inducible-shRNA experiments, doxycycline (DOX, Sigma) was used at 1 µg/mL in culture media and replaced every 2-3 days. Cell viability was analyzed after 4-5 days of DOX treatment using the CellTiter-Glo luminescence assay (Promega), which measures cellular ATP levels as a surrogate for cell number and growth. Luminescence was read on a Tecan M2000 Infinite Pro plate reader. Cells were imaged with a Nikon Eclipse TE2000-U light microscope and SPOT RT3 camera. For iTRAQ, cells were grown on 15-cm plates and harvested when 70-80% confluent for lysis. For SILAC labeling, cells were passaged in heavy, medium, or light media for 7-8 population doublings, and carefully maintained at optimal confluence (70-80%) during passaging before lysis.

Inducible shRNA retroviral constructs

A, B, and D cell lines were sequentially transduced with retroviral constructs for rtTA3 (MSCV-rtTA3-hygro; **Fig. 1A**) and constructs for inducible shKras (27) and shLuc expression,

6

adapted from the TGMP (TRE-GFP-miR30-PGK-Puro[R]) inducible knockdown system

previously described by G. Hannon, S. Lowe, and colleagues (28). 8988T and PANC-1 cells

were transduced with an all-in-one (contains rtTA and TRE-shRNA) inducible knockdown

lentiviral vectors (pLKO-Tet-ON) containing shLACZ.1650 and shKRAS.407 hairpins, which

were previously validated (29) and generously provided by Dr. William Hahn. For double

knockdown experiments, shFAK and shGpr56 were cloned into a TGMB (TRE-GFP-miR30-

PGK-Blast[R]) vector. mir30-based shRNA 97-mers were synthesized (Life Technologies) for

cloning. The individual shRNAs were cloned into the TGMP and TGMB vectors using XhoI and

EcoRI restriction enzyme sites. High-fidelity restriction enzymes and T4 ligase (New England

BioLabs) were used in recommended buffers. The sequences of the shRNA 22-mers and primers

used for shRNA cloning are listed in **Supplementary Table 1**. *MSCV-IRES-GFP* and *MSCV-*

KrasG12D-IRES-GFP retroviral vectors were used for overexpression studies to confirm on-

target Kras knockdown.

Retroviral and lentiviral production and transduction

For retroviral infections, retroviral backbone and pCL-Eco (for mouse cells) were

transfected into 293T cells with TransIT-LT1 (Mirus Bio). For lentiviral infections, lentiviral

backbone, packaging vector (delta8.2 or psPAX2), and envelope (VSV-G) were transfected.

Supernatant was collected at 48 and 72 hours and applied to target cells with 8 μg/mL polybrene

for transduction. Transduced cells were treated with 2 μg/mL puromycin (Life Technologies),

400 μg/mL hygromycin B (Roche), or 10 μg/mL blasticidin S (Life Technologies) for 3-7 days,

as appropriate, for antibiotic selection. To generate single cell clones from the transduced cells,

7

we sorted one cell per well into 96-well plates using a FACSAria II (Becton Dickinson) FACS sorter.

In vitro growth and adherence assays

For growth curves, 250-1000 cells were plated on day 0 and grown for five days in culture. 4-5 replicates for each cell line per day were assessed for cell viability by CellTiter-Glo (Promega). Cell viability results were normalized to luminescence at day 0. For growth curves measured in cell number rather than luminescence, 10,000 cells per well were plated in 6-well plates on day 0 in three replicates, and cells were trypsinized and counted every day. Low-density colony forming assays were performed by plating 1000 cells into 6-well plates in triplicate and staining with 0.5% crystal violet 7-10 days after plating. Cells for clonal efficiency assay were grown in 96-well dishes for 21 days with media supplementation with or without DOX every 2-3 days. Clones were stained with crystal violet and absorbance at 540 nm quantified following solubilization with Sorensen's buffer (0.1M sodium citrate, 50% ethanol, pH 4.2). 3D cultures were established by plating 250-500 cells onto a growth factor-reduced matrigel (Corning) layer, allowing cell migration into matrigel for 4-6 hours. Cells were grown in complete media for 12 days prior to analysis. For adherence assay, single cell suspensions were generated and 5000-10,000 cells were plated in 100 uL media into 96-well plates. After one hour, media was aspirated, and cell viability of remaining adhered cells was analyzed by CellTiter-Glo and compared to cell viability of suspension cells immediately at time of plating. To disrupt actin cytoskeleton, cells were treated with latrunculin B (632 nM) for 1 hour prior to imaging. For anoikis assay, cells were grown as single cell suspension for 48 hours on poly-HEMA (Sigma) coated plates or commercial low-adherence plates (Corning) prior to protein

8

collection for immunoblotting. To determine response to matrigel, suspension cells were assessed for cell viability using CellTiter-Glo.

Immunoblotting

Cells were lysed with ice-cold RIPA buffer (Pierce), supplemented with 0.5 μM EDTA and Halt protease and phosphatase inhibitors (Thermo Scientific), rotated at 4°C for 15-30 minutes to mix, and centrifuged at maximum speed for 15 minutes to collect whole cell lysates. For total pY analysis, cells were lysed by freezing the cell pellet in RIPA buffer (with EDTA and inhibitors) at -80°C overnight to best preserve phosphorylation. Protein concentration was measured with the BCA protein assay (Pierce). 30 μg of total protein per sample was loaded into 4-12% Bis-Tris gradient gels (Life Technologies) and separated by SDS-PAGE. Proteins were transferred to nitrocellulose (for fluorescence detection) or PVDF (for chemiluminescent detection) membranes. The following antibodies were used for immunoblotting: mouse anti-HSP90 (BD #610418, 1:10,000), rabbit anti-β-tubulin (CST 2128, 1:1000), mouse anti-KRAS (SCBT sc-30, 1:200), mouse anti-phosphotyrosine (Millipore 4G10, 1:1000), mouse anti-paxillin (BD #610052, 1:1000), mouse anti-vinculin (Sigma-Aldrich V9131, 1:800), rabbit anti-FAK (Millipore 06-543, 1:1000), rabbit anti-FAK pY397 (Invitrogen 44-624G, 1:1000), rabbit anti-pERK1/2(T202/Y204) (CST 4370, 1:1000), mouse anti-ERK1/2 (CST 9107, 1:1000), rabbit anti-CC3(Asp175) (CST 9664, 1:1000), and rabbit anti-cleaved PARP(Asp214) (CST 9541, 1:1000). HSP90 and β-tubulin were used as loading controls. Primary antibodies were detected with fluorescent-conjugated (LI-COR) or HRP-conjugated (BioRad) secondary antibodies for fluorescent (LI-COR) or chemiluminescent detection (Amersham), respectively. For the phospho-RTK array, 500 μg protein in 250 μl lysis buffer for each sample was incubated with

9

the membrane, and experiment was performed following the protocol provided (R&D Systems mouse proteome profiler phospho-RTK array kit #ARY014).

Immunofluorescence

For immunofluorescent staining of focal adhesion structures, 50,000 (for D line) or 100,000 (for B line) cells were plated on cover slips in 6-well plates, and were grown for 2 days before paraformaldehyde fixation. The fixed cells were then stained with mouse anti-paxillin (BD #610052, 1:500) or mouse anti-vinculin (Sigma-Aldrich V9131, 1:800), along with DAPI (Life Technologies) and Alexa Fluor 555 Phalloidin (ThermoFisher Scientific). The secondary antibody used was donkey anti-mouse IgG (H+L) Alexa Fluor 647 conjugate (ThermoFisher Scientific, 1:250). The stained cells were imagined with Applied Precision DeltaVision Spectris Imaging microscope, and images were deconvoluted with the Softworx deconvolution software.

Focal adhesion analysis and quantitation

Cover slips were coated with 0.1 mg/ml rat tail Collagen I (Corning) diluted in PBS for 1 hour at 37°C followed by 20 µg/ml Fibronectin (Sigma) diluted in PBS for 1 hour at 37°C. Cells were seeded in a density of 60,000 cells per cover slip. Cells were fixed 24 hours after seeding with 4% PFA in PBS and washed twice in 30mM Glycine/PBS for 5 minutes. Cells were permeabilized using 0.2% Triton/PBS for 5 minutes and subsequently washed with TBST followed by blocking in 5% milk powder/TBST for 1 hour at room temperature. Primary antibodies (anti-Vinculin, clone hVin-1, Sigma or anti-Paxillin, clone 349/Paxillin, BD Biosciences) were diluted 1:200 in blocking solution and incubated for 45 minutes at 37°C. Afterwards, the cells were washed 3x for 5 min with blocking solution and then incubated with

10

secondary antibodies (anti-mouse Alexa594 or anti-rabbit Alexa647, Invitrogen) diluted 1:200

and Hoechst diluted 1:1000 in blocking solution for 45 minutes at 37°C. Next, the cells were

washed 3x for 5 min in TBST, 2x in PBS and once in MilliQ water before mounting. Cells were

imaged with an inverted Microscope (TE2000, Nikon) with a 60x Plan Apo 1.40 oil objective

and a Photometric Coolsnap HQ camera.

Focal adhesion analysis was performed using ImageJ (Wayne Rasband, National

Institutes of Health, Bethesda, MD). Briefly, images were background subtracted using the

rolling ball method and then thresholded to generate a binary image. Cell areas without focal

adhesions were masked manually and the focal adhesions were analyzed using the "Analyze

Particles" tool and uploaded into the ROI manager. ROIs were overlaid with the original image

to check for detection accuracy. Wrongly detected focal adhesions were deleted and depending

on the stringency of the thresholding the dilate function was applied to the binary image. Focal

adhesion size and numbers were analyzed. To determine the cell area the cells were outlined and

the total area was measured. This measure was used to normalize the number of focal adhesions

per cell area. For each condition, eight cells and at least 289 individual focal adhesions were

analyzed.

To analyze the percentage of cells with focal adhesions the maximum intensity of all

images were set to a value of 5,000 and cells were categorized into plus focal adhesions or non-

focal adhesions manually. 12 images per conditions were analyzed.

RNA isolation and RNA-sequencing (RNA-Seq) analysis

RNA was isolated from PDAC cells using TRIzol (Life Technologies). cDNA libraries

were prepared using an Illumina TruSeq sample preparation kit with indexed adaptor sequences

11

and polyA selection. Sequencing was performed on an Illumina HiSeq 2000 instrument to

obtain single-end 40-nt reads. Gene expression data has been deposited into the Gene

Expression Omnibus (GEO) with accession number GSE95478. All reads that passed quality

metrics were mapped to the UCSC mm9 mouse genome build (http://genome.ucsc.edu/) using

RSEM (v1.2.12) (http://deweylab.github.io/RSEM/). For pairwise differential expression

analyses, data normalization (MedianNorm) and differential analyses between experimental

conditions were performed using EBSeq v1.4.0

(http://bioconductor.org/packages/release/bioc/html/EBSeq.html). All RNA-Seq analyses were

conducted in the R Statistical Programming language (http://www.r-project.org/). Unsupervised

clustering was performed using a Pearson correlation based pairwise distance measure. Heat

maps were generated using the Heatplus package in R.

High-resolution signature analyses between clones within each cell line were performed

using a blind source separation methodology based on Independent Component Analysis (ICA)

(30). RSEM generated estimated expression counts were upper-quartile normalized to a count of

1000. The R implementation of the core JADE algorithm (Joint Approximate Diagonalization of

Eigenmatrices) (31) was used along with custom R utilities. Signatures were visualized using

the sample-to-signature correspondence schematic afforded by Hinton plots where colors

represent directionality of gene expression (red relatively upregulated, blue relatively

downregulated within each signature) and the size of each rectangle quantifies the gene

expression correlation of a given sample (row) with the gene expression pattern identified by the

signature (column). Each signature is two-sided, allowing for identification of upregulated and

downregulated genes for each signature within each sample. Biologically relevant and

statistically significant signatures were identified using a Mann-Whitney U test.

12

For lncRNA analysis reads were mapped to the mouse genome (release NCBIM37) using Tophat v2.0.4 and gene annotation from Ensembl (release 66, ensemble.org). Differential analyses between Dox and no DOX conditions were performed using Cufflinks v2.0.2. and presented in the format detailed in the cufflinks manual (http://cole-trapnell-lab.github.io/cufflinks/cuffdiff/).

Gene Set Enrichment Analyses (GSEA) were carried out using the pre-ranked mode using log2 fold-change values (for pairwise analyses) or standardized signature correlation scores (for ICA signatures) with default settings (32). Network representations of GSEA results were generated using EnrichmentMap (http://www.baderlab.org/Software/EnrichmentMap) for Cytoscape v3.3.0 (http://www.cytoscape.org) with $p < 0.05$ and FDR<0.25 as cut-offs. Each circle represents a gene set with circle size corresponding to gene set size and intensity corresponding to enrichment significance. Red is upregulated and blue is downregulated. Each line corresponds to minimum 50% mutual overlap with line thickness corresponding to degree of overlap. Cellular processes for gene set clusters were manually curated.

Candidate point mutations in RNA-Seq datasets were called using a pipeline based on the GATK Toolkit (https://software.broadinstitute.org/gatk/). Transcriptomic reads were mapped (to mm9) using the Tophat (v2.0.4) spliced aligner and subjected to local realignment and score recalibration using the GATK Toolkit. Mutations were called in LT DOX samples (individual) against No DOX samples (pooled for individual parental lines) with a minimum base quality threshold of 30. Minimum coverage levels of 8X (no-DOX) and 14X (DOX) were required to evaluate a locus for mutations. Variants were filtered to retain those with representation on both strands. No exonic mutations were found to recur across different pools, and variants found to be common between two samples with the same pool did not exceed a 50% variant frequency

13

threshold. The DOX versus no-DOX variant frequency for these within-pool recurrent variants did not exceed 31%. Genomic annotations were performed using ANNOVAR (http://www.openbioinformatics.org/annovar/).

Computer code for RNA-Seq independent component analyses is available upon request. Other software tools for RNA-Seq analyses, website source, and version numbers are listed above. Gene expression data are archived in GEO with accession number GSE95478.

Quantitative RT-PCR

RNA was reverse transcribed using High-Capacity cDNA Reverse Transcription Kit (Applied Biosystems). Quantitative PCR (qPCR) was performed using Taqman probes (Applied Biosystems). C_t values were measured by a LightCycler 480 Real-Time PCR System (Roche) and relative expression (normalized to TBP or actin) was calculated using the $\Delta\Delta C_t$ method.

Drug treatments

PF562271, PF573228, AZD0530, dasatinib, and SU6656 were purchased from Selleck Chemical. All compounds were diluted to 10 mM stock concentration in DMSO. To generate dose-response curves, cells (250-500 for D clones, 750-1000 for B clones) were plated in 96-well white plates (Perkin Elmer) in 100 μL of media and incubated overnight. 100 μL of drug at 2X final concentration was added to each well in triplicate for each cell line and dose. Cell viability was determined at 72 hours using CellTiter-Glo (Promega). Percent viability was calculated for each dosed well compared to solvent controls (DMSO) and plotted against log10[Dose] (M). For dose-response curves, each replicate for each cell line and dose was plotted along with curve-fit regression for three-component inhibitor response (Prism).

14

Subcutaneous tumor transplant in immunocompromised mice

All animal studies were approved by the MIT Institutional Animal Care and Use Committee. Cells were transplanted to form tumors in NOD/SCID mice (Taconic) via subcutaneous injections. 100 µL of cell suspensions of varying concentrations in cold PBS were injected per tumor to determine tumor-forming capacity and tumor growth kinetics in the context of gene knockdown. Tumor formation was monitored over time by visual observation. Tumor-initiating cell number was calculated based on limiting dilutions of transplanted cells using web-based ELDA software (http://bioinf.wehi.edu.au/software/elda/).

Tumor growth was followed by caliper measurement or luciferase imaging. Caliper measurement was done in 3-4 day intervals. Tumor volume was calculated from caliper measurements using the modified ellipsoid formula: $(length)x(width)^2/2$. Because the PDAC cells are engineered to express *MSCV-Luciferase-IRES-GFP* (plasmids were retrovirally transduced like the inducible shRNA constructs), tumors were measured based on luminescence using IVIS spectrum optical imaging (Xenogen corporation). Bioluminescence imaging by IVIS was done in 3-4 day intervals by injecting 100 µl of 30 mg/ml luciferin per mouse and imaging 10 minutes post-injection. The level of bioluminescence in radiance was analyzed by Living Image software (Perkin Elmer). Cell lines were made from subcutaneous tumors by dissociation using a collagenase IV (Worthington), dispase, trypsin, and DNAse cocktail in HEPES-buffered HBSS.

Phosphotyrosine analysis via LC-MS/MS (iTRAQ)

15

Cells were lysed in 8 M urea (Sigma) and were quantified using BCA assay (Pierce). Proteins were reduced with 10 mM dithiothreitol (Sigma) for 1 hour at 56°C and then alkylated with 55 mM iodoacetamide (Sigma) for 1h at 25°C in the dark. Proteins were then digested with modified trypsin (Promega) at an enzyme/substrate ratio of 1:50 in 100 mM ammonium acetate, pH 8.9 at 25°C overnight. Trypsin activity was halted by addition of acetic acid (99.9%, Sigma) to a final concentration of 5%. After desalting using a C18 Sep-Pak Plus cartridge (Waters), peptides were lyophilized and store at -80°C. Peptides were labeled with iTRAQ 4plex (AB Sciex) as previously described (33). Lyophilized samples (400 μg) were labeled with 1 aliquot of iTRAQ label per peptide sample. Peptides were dissolved in 30 μL of 500 mM triethylammonium bicarbonate, pH 8.5, and each iTRAQ reagent was dissolved in 70μL of isopropanol. Each peptide sample was combined with one of four iTRAQ labels, vortexed, and incubated for 1 hour at 25°C. The labeled peptides were then combined and concentrated to completion.

For immunoprecipitation, protein G agarose (60 μL, Millipore) was incubated with anti-phosphotyrosine antibodies (12 μg 4G10 (Millipore), 12 μg PT66 (Sigma), and 12 μg PY100 (CST)) in 400 μL of IP buffer (100mM Tris, 100mM NaCl, and 1% Nonidet P-40, pH 7.4) for 8 hours at 4°C with rotation. The antibody conjugated protein G was washed with 400 μL of IP buffer. The iTRAQ labeled peptides were dissolved in 400 μL IP buffer and the pH was adjusted to 7.4. The iTRAQ labeled peptides were then incubated with the antibody conjugated protein G overnight at 4°C with rotation. The agarose was washed with 400 μL IP buffer followed by four rinses with 400 μL rinse buffer (100 mM Tris, pH 7.4). Peptides were eluted with 70 μL of 100 mM glycine, pH 2 for 30 minutes at 25°C. Offline immobilized metal affinity chromatography (IMAC) was used to further enrich for phosphotyrosine peptides (33).

16

Peptides were then loaded on a pre-column and separated by reverse phase HPLC using an EASY- nLC1000 (Thermo) over a 140 minute gradient before nanoelectrospray using a QExactive mass spectrometer (Thermo). The mass spectrometer was operated in a data-dependent mode. The parameters for the full scan MS were: resolution of 70,000 across 350-2000 m/z, AGC $3e^6$, and maximum IT 50 ms. The full MS scan was followed by MS/MS for the top 10 precursor ions in each cycle with a NCE of 32 and dynamic exclusion of 30 s. Raw mass spectral data files (.raw) were searched using Proteome Discoverer (Thermo) and Mascot version 2.4.1 (Matrix Science). Mascot search parameters were: 10 ppm mass tolerance for precursor ions; 0.8 Da for fragment ion mass tolerance; 2 missed cleavages of trypsin; fixed modification were carbamidomethylation of cysteine and iTRAQ 4plex modification of lysines and peptide N-termini; variable modifications were methionine oxidation, tyrosine phosphorylation, and serine/threonine phosphorylation. Only peptides with a Mascot score greater than or equal to 25 and an isolation interference less than or equal to 25 were included in the quantitative data analysis. The average false discovery rate was 0.0029 (ranging from 0.0013-0.0041). iTRAQ quantification was obtained using Proteome Discoverer and isotopically corrected per manufacturer's instructions. The iTRAQ values were normalized to the mean relative protein quantification ratios obtained from a total protein analysis. For the total protein analysis, 0.2% of the supernatant from the phosphotyrosine peptide immunoprecipitation was analyzed via LC-MS/MS. This analysis serves as a loading control as it gives quantitation for the most abundant non-phosphorylated peptides. The phosphotyrosine LC-MS/MS analysis was performed three times with different sample preparations. Only tyrosine phosphorylation sites that were detected in at least two independent experiments were considered for further analysis.

17

SILAC analysis

SILAC-labeled cells were cultured at a concentration of 10^6 cells/mL in DMEM medium supplemented with 10% FBS and penicillin/streptomycin, and either normal L-lysine (K0) and L-arginine (R0), or medium-labeled D_4- lysine (K4) and $^{13}C_6$- arginine (R6), or heavy-labeled $^{13}C_6$-$^{15}N_2$ lysine (K8) and $^{13}C_6$-$^{15}N_4$ arginine (R10). Lysine and arginine were supplemented at concentrations of 40 mg/L and 120 mg/L, respectively. Labeled murine PDAC cells (LT DOX or No DOX) were harvested after 7-8 cell doublings.

Cells were washed once with PBS and lysed for 30 min in ice-cold lysis urea buffer (8 M urea; 75 mM NaCl, 50 mM Tris HCl pH 8.0, 1 mM EDTA, 2 µg/mL aprotinin (Sigma, A6103), 10 µg/mL leupeptin (Roche, #11017101001), 1 mM PMSF (Sigma, 78830), 10 mM NaF, 5 mM sodium butyrate, 5 mM iodoacetamide (Sigma, A3221), Phosphatase Inhibitor Cocktail 2 (1:100, Sigma, P5726), Phosphatase Inhibitor Cocktail 3 (1:100, Sigma, P0044). Lysates were centrifuged at 20,000g for 10 min, and protein concentrations of the clarified lysates were measured via BCA assay (Pierce, 23227). A total of 5 mg total proteins per SILAC channel were combined for a total of 15 mg proteins per SILAC experiment.

Protein disulfide bonds of the combined lysates were reduced for 45 min with 5 mM dithiothreitol (Thermo Scientific, 20291) and alkylated for 45 min with 10 mM iodoacetamide. Samples were then diluted 1:4 with 50 mM Tris HCl, pH 8.0, to reduce the urea concentration to 2 M. Lysates were digested for 2 h using 1:50 enzyme-to-substrate ratio LysC (Wako, 129-02541) and trypsin (Promega, V511X) was added in a 1:50 enzyme-to-substrate ratio for digest at room temperature overnight. Peptide mixtures were acidified to a final volumetric concentration of 1% formic acid (Fluka, 56302) and centrifuged at 2,000g for 5 min to pellet urea that had precipitated out of solution. Peptide mixtures were desalted on tC18 SepPak

18

columns (Waters, 500 mg WAT036790). Columns were conditioned with 1×5 ml 100% acetonitrile and 1×5 ml 50% acetonitrile/0.1% formic acid washes, and equilibrated with 4×5 ml 0.1% trifluoroacetic acid (Fluka, TX1276-6). After loading the sample onto the column, samples were desalted with 3×5 ml 0.1% trifluoroacetic acid washes and 1×5 ml 1% formic acid wash. Peptides were eluted from the column with 2×3 ml 50% acetonitrile/0.1% formic acid. Eluted peptide samples were placed in a vacuum concentrator to evaporate the elution solvent and produce purified peptide samples.

To reduce peptide complexity, samples were separated by basic reversed-phase chromatography. For basic RP separation, desalted peptides were reconstituted in 1.8 mL 20 mM ammonium formate, pH 10, and centrifuged at $10,000g$ to clarify the mixture before it was transferred into autosampler tubes. Basic reversed-phase chromatography was conducted on a 9.4 mm $\times$ 250 mm column Zorbax 300 Å Extend-C18 column (Agilent, 5 μm bead size), using an Agilent 1100 Series HPLC instrument. Solvent A (2% acetonitrile, 5 mM ammonium formate, pH 10), and a nonlinear increasing concentration of solvent B (90% acetonitrile, 5 mM ammonium formate, pH 10) were used to separate peptides by their hydrophobicity at a high pH. We used a flow rate of 3 ml/min and increased the percentage of solvent B in a nonlinear gradient with 4 different slopes (0% for 2 min; 0% to 10% in 5 min; 10% to 27% in 34 min; 27% to 31% 4 min; 31% to 39% in 4 min; 39% to 60% in 7 min; 60% for 8 min). Eluted peptides were collected in 96 $\times$ 2 mL deepwell plates (Whatman, #7701-5200) with 1 min (= 1 ml) fractions for the 4.6 mm column and 40 s (= 2 ml) fractions for the 9.4 mm column. Early eluting peptides were collected in fraction "A", which is a combined sample of all fractions collected before any major UV-214 signals were detected.

19

Peptide samples were combined into 24 subfractions, respectively, to be used for

proteome analysis. Subfractions were achieved by combining every 24th fraction (1,25,49;

2,26,50; ...). Subfractions were acidified to a final concentration of 1% formic acid, and 5% of

the volumetric samples were reserved for proteome analysis.

The remaining 95% of each of the original 72 subfractions from bRP (above) were

further combined before enrichment for PTM analyses as follows: every 12th fraction was

combined (1,13; 2,14; ...) to generate 12 fractions. Peptide fractions were subsequently dried by

vacuum sublimation in a vacuum concentrator. We have also analyzed an early eluting

hydrophilic fraction labeled fraction A which contains a large number of multiply

phosphorylated peptides.

As described previously (34), iron-chelated IMAC beads were prepared from Ni-NTA

superflow agarose beads (Qiagen, #1018611) that were stripped of nickel with 100 mM EDTA

and incubated in an aqueous solution of 10 mM $FeCl_3$ (Sigma, 451649). Dried phosphopeptide

fractions were reconstituted in 50% acetonitrile/0.1% trifluoroacetic acid and then diluted 1:1

with 100% acetonitrile/0.1% trifluoroacetic acid to obtain a final 80% acetonitrile/0.1% TFA

peptide solution at a concentration of 0.5 μg/μl. Peptide mixtures were enriched for

phosphorylated peptides with 10 μL IMAC beads for each sample for 30 min. Enriched IMAC

beads were loaded on Empore C18 silica-packed stage tips (3M, 2315). Stage tips were

equilibrated with 2×100 μL washes of methanol, 2×50 μL washes of 50% acetonitrile/0.1%

formic acid, and 2×100 μL washes of 1% formic acid. Samples were then loaded onto stage

tips and washed twice with 50 μL of 80% acetonitrile/0.1% trifluoroacetic acid and 100 μL of

1% formic acid. Phosphorylated peptides were eluted from IMAC beads with 3×70 μL washes

of 500 mM dibasic sodium phosphate, pH 7.0, (Sigma, S9763) and washed twice with 100 μL of

20

1% formic acid before being eluted from stage tips with 60 μL 50% acetonitrile/0.1% formic

acid. All washes were performed on a tabletop centrifuge at a maximum speed of 3,500*g*.

All peptide samples were separated on an online nanoflow EASY-nLC 1000 UHPLC

system (Thermo Fisher Scientific) and analyzed on a benchtop Orbitrap Q Exactive mass

spectrometer (Thermo Fisher Scientific). Ten percent of each proteome (containing ~1 μg) and

fifty percent of each phosphopeptide, K(GG) peptide, and K(Ac) peptide sample were injected

onto a capillary column (Picofrit with 10 μm tip opening / 75 μm diameter, New Objective,

PF360-75-10-N-5) packed in-house with 20 cm C18 silica material (1.9 μm ReproSil-Pur C18-

AQ medium, Dr. Maisch GmbH, r119.aq). The UHPLC setup was connected with a custom-fit

microadapting tee (360 μm, IDEX Health & Science, UH-753), and capillary columns were

heated to 50 °C in column heater sleeves (Phoenix-ST) to reduce backpressure during UHPLC

separation. Injected peptides were separated at a flow rate of 200 nL/min with a linear 80 min

gradient from 100% solvent A (3% acetonitrile, 0.1% formic acid) to 30% solvent B (90%

acetonitrile, 0.1% formic acid), followed by a linear 6 min gradient from 30% solvent B to 90%

solvent B. Each sample was run for 150 min, including sample loading and column equilibration

times. Data-dependent acquisition was obtained using Xcalibur 2.2 software in positive ion

mode at a spray voltage of 2.00 kV. MS1 Spectra were measured with a resolution of 70,000, an

AGC target of 3e6 and a mass range from 300 to 1800 *m/z*. Up to 12 MS2 spectra per duty cycle

were triggered at a resolution of 17,500, an AGC target of 5e4, an isolation window of 2.5 *m/z*

and a normalized collision energy of 25. Peptides that triggered MS2 scans were dynamically

excluded from further MS2 scans for 20 s.

All mass spectra were analyzed with MaxQuant software version 1.3.0.5 using a mouse

UniProt database. MS/MS searches for the proteome data sets were performed with the

21

following parameters: Oxidation of methionine and protein N-terminal acetylation as variable

modifications; carbamidomethylation as fixed modification. For IMAC data sets

phosphorylation of serine, threonine and tyrosine residues were searched as additional variable

modifications. Trypsin/P was selected as the digestion enzyme, and a maximum of 3 labeled

amino acids and 2 missed cleavages per peptide were allowed. The mass tolerance for precursor

ions was set to 20 p.p.m. for the first search (used for nonlinear mass re-calibration) and 6 p.p.m.

for the main search. Fragment ion mass tolerance was set to 20 p.p.m. For identification we

applied a maximum FDR of 1% separately on protein, peptide and PTM-site level. We required

2 or more unique/razor peptides for protein identification and a ratio count of 2 or more for

protein quantification per replicate measurement. PTM-sites were considered to be fully

localized when they were measured with a localization probability >0.75 in each of the three

replicates. To assign regulated proteins and PTM-sites we used the Limma package in the R

environment to calculate moderated t-test Pvalues corrected by the Benjamini Hochberg method,

as described previously[48]. Bland-Altman filtering was applied at 99.9% (+/-3.29 sigma).

Combined analysis of SILAC and iTRAQ data

To ensure the identification of critical pathways that mediate the response to Kras

inhibition with minimal clonal or technical confounding effects, we only included peptides that

were called in at least two replicates of iTRAQ experiments and showed significant correlation

in the up and down-regulated genes ($\geq$2-fold for SILAC, $\geq$1.2-fold for iTRAQ) in the Kras-

inhibited cells in both clones (p<0.0001, Pearson correlation).

Statistical analyses

22

P-values for comparisons of two groups were determined by two-tailed Student's t-test (for normally distributed data) or Mann-Whitney U-test (for non-parametric data), as noted in the figure legends. Chi-square analysis was performed for statistical evaluation of clonal efficiency. Pearson correlations were calculated for scatter plots of phosphoproteomic and proteomic data (Prism). All replicates were included in these analyses. A p-value of <0.05 was used to denote statistical significance. All error bars denote 95% confidence intervals, standard error of mean (s.e.m.), or standard deviation (s.d.), as noted in the figure legends.

23

RESULTS

Temporal control of endogenous *Kras* expression in PDAC cells

To elucidate the consequence of inhibiting endogenous *Kras* in PDAC, we first derived

cell lines from three distinct primary tumors (labelled A, B, and D) from an autochthonous

PDAC mouse model (*Pdx1-CreER; Kras$^{LSL-G12D/+}$; p53$^{flox/flox}$*), which recapitulates the biology of

human PDAC (13). We used murine cells with defined genetic alterations frequently observed

in human PDACs (*Kras* and *p53*) (6,35) to minimize genetic variability in our analyses. We

transduced these cell lines with a doxycycline-inducible shRNA-mediated knockdown system

that enables the temporal control of endogenous *Kras* expression (**Fig. 1A and Supplementary**

Table 1). Here, partial inhibition and the subsequent reactivation of endogenous *Kras* are

achieved by administration and withdrawal of doxycycline (DOX). We employed two DOX-

inducible miR30-based hairpins targeting the 3'-UTR of *Kras* (shKras.1442 or shKras.923) or a

control hairpin targeting firefly *luciferase* (shLuc). These Kras hairpins do not distinguish

between wild-type and mutant alleles of *Kras* due to 3'-UTR targeting. Following retroviral

transduction, we selected for cells with robust hairpin expression by 24-48 hours of DOX

treatment (prior to visible phenotypic consequences of Kras knockdown) to induce concomitant

expression of a GFP reporter and the hairpin, and isolated single cell clones that express GFP at

the highest levels by FACS. Finally, we confirmed on-target Kras protein and mRNA

knockdown at >70% in these clones under DOX treatment (**Figs. 1B-C, Supplementary Figs.**

1A-C).

Murine PDAC cells tolerate stable Kras knockdown *in vitro* and *in vivo*

Rather than undergoing permanent growth arrest or apoptosis, all PDAC cells analyzed tolerated acute and sustained Kras knockdown and continued to proliferate *in vitro*. Short-term DOX treatment for 3-5 days ("ST DOX") of shKras-expressing cells, but not shLuc-expressing cells, resulted in significantly altered cell morphology and decreased proliferation, consistent with a partial requirement of endogenous *Kras* expression for PDAC maintenance (**Figs. 1D-E**). Under prolonged DOX treatment for >21 days ("LT DOX"), shKras-expressing cells retained GFP and shKras hairpin expression, and demonstrated persistent Kras knockdown (**Figs. 1B-C**). LT DOX cells continued to proliferate with slower kinetics than untreated cells ("No DOX") and maintained morphological changes (**Figs. 1E-F**).

To examine the requirement of endogenous *Kras* for PDAC maintenance *in vivo*, we transplanted untreated shKras-transduced cells subcutaneously into nude mice, allowed tumors to form, and induced hairpin expression with DOX food. Acute *Kras* knockdown in established tumors resulted in decreased tumor growth and even tumor regression, attributable in part to decreased proliferation as evident by reduced BrdU incorporation (**Supplementary Figs. 2A-C**). Despite long-term DOX treatment of mice (>6 weeks; LT DOX), tumors grew at decreased rates compared to untreated tumors and retained GFP expression (**Supplementary Fig. 2D**). Taken together, these observations suggest that endogenous levels of *Kras* expression are not essential for maintaining murine PDAC cell proliferation and survival *in vitro* or *in vivo*.

Response to Kras knockdown is adaptive and reversible

It is generally thought that cancer cells gain resistance to oncogene inhibition through elimination of a sensitive cell population and outgrowth of a resistant population. Given the lack

25

of significant apoptosis with acute and sustained Kras knockdown and the rapid conversion of

cell morphology, we hypothesized that murine PDAC cells underwent adaptation to a state

tolerant to Kras inhibition rather than selection of rare cells intrinsically resistant to Kras

knockdown. To distinguish between these two possibilities, we analyzed the number of single

cell clones that could grow from shKras-transduced cell lines in the absence or presence of

sustained DOX treatment. If there were a selection process, we would expect to see a marked

decrease in the number of clones that formed under prolonged DOX treatment. Alternatively, if

adaptation occurred, then the same number of clones should form regardless of DOX treatment

condition. While we observed differences between parental cell lines, the vast majority of clones

were able to expand despite sustained Kras knockdown (**Fig. 2A**), suggesting adaptation to a

state tolerant to Kras inhibition (Kras-inhibited state). All colonies that did form in DOX were

smaller in size, consistent with the expected decreased proliferative rate following Kras

knockdown (**Fig. 2B**). Indeed, when we removed DOX to restore Kras levels (**Fig. 2C**), cells

rapidly reverted morphological phenotypes and proliferative kinetics (**Figs. 2D-E**). Finally, cells

were re-sensitized to DOX treatment in terms of proliferative and morphological phenotypes

(**Fig. 2F**). Collectively, these observations indicate that murine PDAC cells respond to partial

Kras inhibition by a reversible cell state change.

Diminished *in vivo* tumor initiating capacity following stable Kras inhibition

While Kras inhibition did not significantly block the ability of PDAC clones to form in

2D cultures (**Fig. 2A**), we also interrogated the tumorigenic ability of Kras-inhibited cells in 3D

culture *in vitro* and in immunocompromised mice *in vivo*, as Kras has been implicated in

maintaining tumor-initiating cells (TICs) or stemness (36). Interestingly, Kras-inhibited cells

26

retained the ability to form 3D tumorspheres in matrigel *in vitro* (**Fig. 3A**) in similar relative

frequencies to 2D clonal cultures (**Fig. 2A**), though the spheres that formed were smaller,

consistent with a proliferative defect (**Fig. 3B**). In contrast, Kras-inhibited cells exhibited

reduced TICs in forming subcutaneous tumors *in vivo* (**Fig. 3C and Supplementary Table 2**).

However, tumors did form from LT DOX-treated shKras-expressing cells. Sustained Kras

inhibition was maintained even in secondary cell lines (**Fig. 3D**), which exhibited comparable

levels of Kras protein and mRNA knockdown to that of the primary cell lines (**Fig. 3E-F**).

Collectively, these data suggest that sustained Kras inhibition can reduce cell proliferation *in*

vitro and *in vivo* and impair TICs *in vivo*, confirming that Kras is a valuable therapeutic target.

Nonetheless, Kras inhibition did not ablate the tumorigenic ability of murine PDAC cells.

The Kras-inhibited state does not display significant alterations in gene expression

We next sought to understand the molecular and biochemical changes associated with the

Kras-inhibited state, which may reveal targetable mechanisms of resistance. To identify

transcriptional changes associated with adaptation to this state, we performed RNA-sequencing

on polyA-selected RNA from six shKras-transduced Kras-inhibited and -uninhibited subclone

pairs (2 per primary cell line A, B, and D) and a control shLuc-transduced pair. We verified data

quality by confirming *Kras* knockdown and identifying the engineered C→T *G12D Kras* gene

mutation in the transcript sequencing reads. We did not identify recurrent non-synonymous

mutations in exonic regions in the Kras-inhibited cells (**Supplementary Table 3**). Strikingly,

we also did not observe significant differences in coding gene or lncRNA expression between the

baseline and Kras-inhibited states (**Supplementary Tables 4 and 5**). Indeed, unsupervised

hierarchical clustering demonstrated that gene expression differences were driven more strongly

27

by parental cell line and subclonal identity rather than alterations in the *Kras* expression state (**Fig. 4A**).

To account for clonal variability and to derive a robust gene signature associated with the Kras-inhibited state using an unbiased approach, we employed a blind-source separation method termed independent component analysis (ICA). This separation technique not only derived gene expression signatures associated with individual parental cell lines or clones, but also identified signature profiles that distinguished the independent gene expression changes associated with Kras knockdown and DOX treatment (using the shLuc control cell line treated with DOX) (**Figs. 4B-D**). It became readily apparent that DOX treatment alone could have significant effects on gene expression independent of Kras knockdown in our cell lines. For example, the G-protein coupled receptor *Gpr56* was strongly upregulated by DOX (**Supplementary Table 3**) and was significantly associated with the DOX signature but not the Kras knockdown signature (z-scores of 7.32 and -0.51, respectively). We confirmed that *Gpr56* represented an endogenous eukaryotic target of the prokaryotic protein rtTA in the presence of DOX (**Supplementary Figs. 3A-C**). As expected, *Gpr56* knockdown did not impact the proliferative or morphological phenotypes of Kras-inhibited cells (**Supplementary Figs. 3D-E**). This ability to distinguish a DOX-regulated gene from a Kras-regulated gene demonstrates the power of ICA to identify functionally important gene signatures. Furthermore, genes in the Kras knockdown signature were specifically and significantly, although not strongly, enriched in Kras-inhibited cells (**Fig. 4D**). Comparison of the degree of transcriptional alterations associated with either DOX treatment or Kras knockdown suggested that stable Kras inhibition does not lead to striking gene expression changes (**Figs. 4C-D**), contrary to what one might expect as Kras-mediated signal

28

transduction ultimately regulates nuclear transcriptional activity. These observations suggest

that the Kras-inhibited state is not strongly dependent on mutational or transcriptional alterations.

To elucidate potential Kras-regulated transcriptional pathways or functionally important

pathways that maintain cell viability in the Kras-inhibited state, we performed gene set

enrichment analysis (GSEA) on the Kras knockdown signature. While few genes sets in

MSigDB were significantly associated with the Kras knockdown signature, network correlation

analysis revealed enrichment of gene sets associated with receptor tyrosine kinase (RTK),

PI3K/AKT signaling, receptor endocytosis and recycling, and redox metabolism in Kras-

inhibited cells (**Fig. 4E**), possibly because these compensatory pathways are upregulated in

response to Kras inhibition to support the steady-state proliferation of PDAC cells.

Global phosphoproteomic profiling reveals enhanced focal adhesion signaling in the Kras-inhibited state

We hypothesized that signaling flux through alternative pro-proliferation and pro-

survival pathways may underlie the adaptive state. Importantly, identification of compensatory

pathways could uncover potentially druggable protein targets for PDAC therapy. We first

examined signaling differences between the Kras-uninhibited and -inhibited states in a tyrosine-

focused fashion, because the best-characterized upstream regulators of Kras-mediated signal

transduction are RTKs and genes associated with RTK signaling are enriched in the Kras

knockdown signature (**Fig. 4E**). Assessment of global tyrosine phosphorylation levels (**Fig. 5A**)

showed an overall increase in the levels of tyrosine phosphorylation in Kras-inhibited cells,

suggestive of increased activation of tyrosine kinase-mediated pathways that may compensate

for decreased Kras levels. However, a limited phospho-RTK array did not reveal candidate

29

upstream regulators mediating the adaptive state change (**Supplementary Fig. 4A**). Therefore, we employed two distinct approaches for unbiased global phosphoproteomic analysis: stable isotope labeling by amino acids in cell culture (SILAC) and isobaric tag for relative and absolute quantitation (iTRAQ). The SILAC approach (34) enables analysis of serine-, threonine-, and tyrosine-phosphorylated peptides (pS, pT, and pY, respectively) as well as total proteome changes. As a complementary approach, we adopted an optimized iTRAQ protocol to enrich specifically for the lowly abundant tyrosine-phosphorylated peptides (33), enhancing the resolution of tyrosine kinase signaling analysis of the Kras-inhibited state (**Supplementary Fig. 4B**). Combining these two approaches, we cross-compared candidate signaling pathways specifically activated or inhibited in the Kras-inhibited state.

Total proteome differences between Kras-uninhibited and Kras-inhibited states showed minimal overall protein abundance alterations by SILAC (**Supplementary Figs. 5A-B and Supplementary Table 6**), consistent with the paucity of transcriptional changes. Importantly, one of the few proteins whose abundance was significantly altered in the Kras-inhibited state was Kras itself (reduced by 60%). Conversely, the highest upregulated protein was the DOX-inducible gene *Gpr56*. For iTRAQ, each experimental replicate identified a robust number of pY peptides that were called with stringent criteria, and at least 230 overlapping pY peptides were identified in more than two replicates (**Fig. 5B and Supplementary Tables 7-9**). Additionally, the signaling changes that occurred in the two independent evaluated clones, B (B shKras.1442 cl2) and D (D shKras.923 cl1), exhibited reasonable correlation (**Figs. 5C-D**), suggesting that the clonal and parental cell line differences were small.

We next performed combined analysis of phosphoprotein abundance from SILAC and iTRAQ data, and found that multiple sites on focal adhesion-associated proteins showed

30

increased phosphorylation (**Fig. 5C**). Examples included Src, focal adhesion kinase (FAK), tensin, paxillin, talin, and vinculin, among many others (**Fig. 5C**). Furthermore, despite the low abundance of pY residues in the total phosphoproteome, our SILAC analysis identified 20-30 pY peptides that overlapped with iTRAQ analysis (**Supplementary Fig. 5C**). Phosphosites on proteins associated with adhesion pathways also exhibited significant upregulation in the SILAC analysis (**Fig. 5D and Supplementary Table 10**). Collectively, these signaling changes suggest that the Kras-inhibited state is characterized by enhanced focal adhesion signaling. Accordingly, immunofluorescent staining for the focal adhesion protein vinculin confirmed markedly enhanced focal adhesion structures in Kras-inhibited cells (**Figs. 6A-C**). Therefore, a major feature of the Kras-inhibited state is the upregulation of focal adhesion pathway signaling.

The Kras-inhibited state depends on cell attachment

Given enhanced focal adhesion signaling and structures in Kras-inhibited cells, we hypothesized that Kras-inhibited cells are more dependent on attachment for survival. Kras-inhibited cells exhibited enhanced cell attachment capacity, demonstrated by faster adherence to culture dishes than uninhibited cells (**Fig. 6D**). This property likely underlies the greater resistance of Kras-inhibited cells to actin polymerization inhibitor latrunculin B-induced detachment (**Fig. 6E**). Moreover, Kras-inhibited cells were more sensitive to anoikis, as evident by increased induction of apoptosis in non-adherent culture conditions (**Fig. 6F**). Conversely, Kras-inhibited cells exhibited significantly enhanced viability in suspension when the media was supplemented with extracellular matrix proteins (**Fig. 6G**). Overall, analyses of the cell biological features of Kras-inhibited cells reveal enhanced adherence properties and an increased dependency on adhesion for cell viability *in vitro*.

31

To determine the relevance of our findings to human PDAC, we introduced DOX-inducible hairpins targeting LACZ (control) or KRAS into 8988T and PANC1 human PDAC cell lines, which we and others have previously shown tolerate KRAS inhibition (15,16,37). Consistent with observations in murine cells, KRAS knockdown in human PDAC cell lines (**Fig. 7A, Supplementary Fig. 6A**) resulted in morphological changes and decreased proliferation that were reversible by KRAS reactivation (**Figs. 7B-D, Supplementary Figs. 6B-D**). Additionally, 8988T cells in the KRAS-inhibited state exhibited increased sensitivity to anoikis (**Fig. 7E**) and enhanced focal adhesion structures (**Figs. 7D, 7F, and 7G**), indicative of dependency on cell attachment. While KRAS-inhibited PANC1 cells did not display increased anoikis sensitivity (**Supplementary Fig. 6E**), they showed enhanced focal adhesion structures (**Supplementary Figs. 6D, 6F, and 6G**). The variability in response on focal adhesion formation and dependence observed in human PDAC cells compared to the murine models likely emerge from the greater heterogeneity (e.g. genetic, phenotypic) seen in human PDAC. Nonetheless, these results reveal that our findings in murine PDAC cells are relevant to at least a subset of human PDAC cells.

Genetic or pharmacological inhibition of FAK does not impair survival of Kras-inhibited PDAC cells

We hypothesized that direct inhibition of focal adhesion kinase (FAK) may target a unique vulnerability in the context of Kras inhibition, and interrogated the requirement of FAK-mediated signaling in maintaining Kras-inhibited cell viability. Kras-inhibited cells did not show increased sensitivity compared to uninhibited cells to pharmacological inhibition of FAK or the central upstream regulator of the focal adhesion signaling pathway Src (**Supplementary Fig. 7**). As both FAK and Src integrate multiple signaling pathways and the off-target effects of

32

pharmacological inhibitors could mask differential sensitivity, we performed more-specific

shRNA-mediated knockdown of FAK (**Supplementary Fig. 8A**). Even though FAK

knockdown disrupted the polarity and organization of focal adhesion plaques, it did not ablate

the formation of these structures in Kras-inhibited cells (**Supplementary Fig. 8B**). Moreover,

FAK knockdown did not synergize with Kras knockdown to further impair proliferation *in vitro*

or subcutaneously transplanted tumor growth *in vivo* (**Supplementary Fig. 8C and**

Supplementary Figs. 9A-E). These data suggest that there may be compensatory mechanisms

to maintain focal adhesions upon FAK inhibition. While FAK inhibition was insufficient to

impair Kras-inhibited cell survival, blockade of the cell adhesion phenotype through alternative

means may still offer a tractable therapeutic strategy.

DISCUSSION

We interrogated the requirement of endogenous *Kras* for maintaining murine PDAC cell

survival with an inducible shRNA-based knockdown system. Surprisingly, our results

demonstrated only a partial requirement of *Kras* for PDAC maintenance. Not only were PDAC

cells able to proliferate under sustained *Kras* knockdown, but they also retained oncogenic

capabilities *in vitro* and *in vivo*. The majority of murine PDAC cells tolerated acute and

sustained Kras inhibition by adapting to a reversible state. The lack of significant mutational and

gene expression changes indicated that such resistance to Kras inhibition was non-genetic and

non-transcriptional. Global phosphoproteomic analyses confirmed that the Kras-inhibited state

was a result of rewiring of signaling through alternative pathways. Specifically, Kras-inhibited

PDAC cells exhibited upregulation of focal adhesion signaling and enhanced adherence

properties and dependence. Due to possible compensatory mechanisms, inhibition of FAK or

33

Src alone was insufficient to selectively impair Kras-inhibited cell survival. Nevertheless, components of this pathway could be novel drug targets for rational combination therapies.

Unlike its well-established role as the driver of PDAC initiation, whether endogenous oncogenic *Kras* is required for PDAC maintenance has remained a longstanding question. To elucidate the dependency of PDAC cells on Kras for survival, we employed an *in vitro* system that allows reversible Kras knockdown to mimic the effect of a non-specific pharmacological Kras inhibitor. It is possible that mutant Kras-specific inhibition could have differential effects from combined inhibition of both alleles, since wild-type Kras has been shown to act as either a tumor suppressor (38) or oncogenic driver (i.e. through amplification) (39–41) in different cancer types. However, the vast majority of approaches currently being developed to inhibit KRAS are not allele-specific (8), thus our system can be utilized to predict mechanisms of resistance to these inhibitors.

Our approach has several advantages over previous work to understand the requirement of Kras for PDAC maintenance and potential mechanisms of resistance to Kras inhibition. Early studies used constitutive RNAi to knockdown Kras in human PDAC cell lines and correlate dependency with gene expression. These experiments defined human PDAC cell lines with variable dependencies on *Kras* for survival following short-term inhibition, but the effects of sustained knockdown, as would more closely mimic treatment of patients, were undefined (15,16). More recent work used a doxycycline-inducible RNAi approach to knockdown Kras in human PDAC cell lines and established human tumor xenotransplants. While comparable decreased *in vitro* proliferation and slower tumor growth *in vivo* were observed, signaling studies were limited to the study of well-defined MAPK and PI3K pathways (42). Recent *in vivo* studies aimed to characterize the requirement of sustained oncogenic *Kras* expression for pancreatic

34

cancer maintenance have employed elegant mouse models engineered to express an inducible oncogenic *Kras* transgene (9,11,12). Because oncogenic *Kras* alone induces PDAC with low frequency and long latency, these models require additional tumor suppressor inactivation or pancreatitis induction to facilitate PDAC development. In these models, withdrawal of oncogenic *Kras* transgene expression in established PDAC tumors led to an initial tumor regression due to apoptosis, but tumor relapse was observed after a period of dormancy (9,11,12,17,18). While these studies provide invaluable insights into the requirement of oncogenic Kras for tumor maintenance, care must be taken into extrapolating the effects of overexpression of an oncogenic *Kras* transgene to explain its endogenous functions. Finally, CRISPR-mediated ablation of endogenous Kras in human and murine PDAC cells demonstrated that Kras is dispensable for survival in a subset of PDAC cells, and that Kras-deficient cells exhibited increased dependency on PI3K signaling (37). However, achieving complete pharmacological inhibition of KRAS is challenging. Furthermore, CRISPR-mediated knockout is irreversible, impairing the ability to distinguish between clonal selection and adaptation as modes of resistance.

Consistent with results from these previous studies, we found that PDAC cells can bypass *Kras* oncogene addiction by adapting to a reversible Kras-inhibited state. Conventionally, it is thought that resistance to cancer therapies occurs by selection of rare cells. Our observations support the emerging view that non-genetic resistance mechanisms can be equally relevant (19,20). Given the significant investment into the development of KRAS inhibitors, advanced knowledge of these resistance mechanisms would facilitate the clinical translation of novel inhibitors and overcome the limitations of single-agent therapy.

35

Unbiased phosphoproteomic analyses of the Kras-inhibited state uncovered increased focal adhesion signaling as a possible resistance mechanism to Kras inhibition. This intriguing finding led us to explore the benefit of targeting FAK in Kras-inhibited PDAC cells. FAK is the central kinase of focal adhesion signaling, and is known to integrate adhesion- and growth factor-dependent signals to regulate cell adhesion, motility, and survival (43,44). Interestingly, *FAK* overexpression in human cancers is often associated with worse prognosis (45,46). Furthermore, FAK interacts with multiple regulators and effectors of KRAS. It has been suggested that KRAS-mediated activation of MEK1 results in phosphorylation of FAK at Ser910, which decreases FAK kinase activity (47). Moreover, FAK inhibition has been shown to suppress the growth of xenograft PDAC tumors with gemcitabine treatment (48). Together, the connection between FAK and KRAS-mediated signaling as well as its implication in human cancers made FAK an appealing target. Unfortunately, as focal adhesion signaling involves multiple inputs and outputs, FAK inhibition alone was insufficient to impair Kras-inhibited cell survival. Nevertheless, identification of the critical nodes of focal adhesion signaling that underlie resistance to KRAS inhibition may inform rational therapeutic combinations with novel KRAS inhibitors.

In summary, we have employed a conditional RNAi system to study the requirement of endogenous *Kras* in PDAC maintenance, and performed unbiased gene expression and phosphoproteomic analyses to characterize the adaptive and reversible Kras-inhibited state. Our observations have important therapeutic implications. First, by showing that the majority of cells could tolerate an approximately 70% inhibition of Kras, it is possible that a KRAS-directed inhibitor needs to achieve near-complete inhibition of KRAS function to exhibit significant clinical impact. Alternatively, multiple nodes of KRAS signaling may need to be inhibited to

36

achieve greater efficacy. Second, even if an effective KRAS inhibitor is successfully developed, resistance may develop. Since PDAC cells can circumvent Kras inhibition via an adaptive and reversible state change, intermittent dosing of a KRAS-directed inhibitor to allow for re-treatment response may be beneficial. Finally, the Kras-inhibited state is characterized by signaling alterations, so targeting compensatory pathways with KRAS inhibition could be a useful therapeutic strategy.

ACKNOWLEDGEMENTS

P-Y.C., M.D.M., and T.J. designed the study; P-Y.C., M.D.M., K.J.D., R.R., A.R., P.M, J.Q., and A.C.S. performed experiments; A.B. conducted bioinformatics analyses; P-Y.C., M.D.M., and T.J. wrote the manuscript.

37

REFERENCES

1. Ryan DP, Hong TS, Bardeesy N. Pancreatic Adenocarcinoma. NEJM. 2014;371:1039–49.

2. American Cancer Society. Cancer Facts and Figures 2017. 2017;Atlanta: A.

3. Conroy T, Desseigne F, Ychou M, Bouché O, Guimbaud R, Bécouarn Y, et al. FOLFIRINOX versus gemcitabine for metastatic pancreatic cancer. N Engl J Med. 2011;364:1817–25.

4. Von Hoff DD, Ervin T, Arena FP, Chiorean EG, Infante J, Moore M, et al. Increased Survival in Pancreatic Cancer with nab-Paclitaxel plus Gemcitabine. N Engl J Med. 2013;369:1691–703.

5. Jones S, Zhang X, Parsons DW, Lin JC-H, Leary RJ, Angenendt P, et al. Core signaling pathways in human pancreatic cancers revealed by global genomic analyses. Science. 2008;321:1801–6.

6. Waddell N, Pajic M, Patch A, Chang DK, Kassahn KS, Bailey P, et al. Whole genomes redefine the mutational landscape of pancreatic cancer. Nature. 2015;518:495–501.

7. Bardeesy N, DePinho R. Pancreatic cancer biology and genetics. Nat Rev Cancer. 2002;2:897–909.

8. Cox AD, Fesik SW, Kimmelman AC, Luo J, Der CJ. Drugging the undruggable RAS: Mission Possible? Nat Rev Drug Discov. Nature Publishing Group; 2014;13:828–51.

9. Collins MA, Bednar F, Zhang Y, Brisset J, Galbán S, Galbán CJ, et al. Oncogenic Kras is required for both the initiation and maintenance of pancreatic cancer in mice. J Clin Invest. 2012;122:639–53.

10. Hingorani SR, Wang L, Multani AS, Combs C, Deramaudt TB, Hruban RH, et al. Trp53R172H and KrasG12D cooperate to promote chromosomal instability and widely metastatic pancreatic ductal adenocarcinoma in mice. Cancer Cell. 2005;7:469–83.

11. Ying H, Kimmelman AC, Lyssiotis C a., Hua S, Chu GC, Fletcher-Sananikone E, et al. Oncogenic kras maintains pancreatic tumors through regulation of anabolic glucose metabolism. Cell. Elsevier Inc.; 2012;149:656–70.

12. Collins MA, Brisset JC, Zhang Y, Bednar F, Pierre J, Heist KA, et al. Metastatic Pancreatic Cancer Is Dependent on Oncogenic Kras in Mice. PLoS One. 2012;7.

13. Friedlander SYG, Chu GC, Snyder EL, Girnius N, Dibelius G, Crowley D, et al. Context-Dependent Transformation of Adult Pancreatic Cells by Oncogenic K-Ras. Cancer Cell. 2009;16:379–89.

14. Hingorani SR, Petricoin EF, Maitra A, Rajapakse V, King C, Jacobetz M a., et al. Preinvasive and invasive ductal pancreatic cancer and its early detection in the mouse. Cancer Cell. 2003;4:437–50.

15. Singh A, Greninger P, Rhodes D, Koopman L, Violette S, Bardeesy N, et al. A Gene Expression Signature Associated with "K-Ras Addiction" Reveals Regulators of EMT and Tumor Cell Survival. Cancer Cell. Elsevier Ltd; 2009;15:489–500.

16. Collisson E a, Sadanandam A, Olson P, Gibb WJ, Truitt M, Gu S, et al. Subtypes of pancreatic ductal adenocarcinoma and their differing responses to therapy. Nat Med.

Nature Publishing Group; 2011;17:500–3.

17.   Kapoor A, Yao W, Ying H, Hua S, Liewen A, Wang Q, et al. Yap1 activation enables bypass of oncogenic KRAS addiction in pancreatic cancer. Cell. Elsevier Inc.; 2014;158:185–97.

18.   Viale A, Pettazzoni P, Lyssiotis C a., Ying H, Sánchez N, Marchesini M, et al. Oncogene ablation-resistant pancreatic cancer cells depend on mitochondrial function. Nature. 2014;514:628–32.

19.   Sun C, Wang L, Huang S, Heynen GJJE, Prahallad A, Robert C, et al. Reversible and adaptive resistance to BRAF(V600E) inhibition in melanoma. Nature. Nature Publishing Group; 2014;508:118–22.

20.   Hata AN, Niederst MJ, Archibald HL, Gomez-Caraballo M, Siddiqui FM, Mulvey HE, et al. Tumor cells can follow distinct evolutionary paths to become resistant to epidermal growth factor receptor inhibition. Nat Med. 2016;22:262–9.

21.   Burrell RA, Swanton C. Tumour heterogeneity and the evolution of polyclonal drug resistance. Mol. Oncol. 2014. page 1095–111.

22.   Pribluda A, de la Cruz C, Jackson E. Intratumoral Heterogeneity: From Diversity Comes Resistance. Clin Cancer Res. 2015;21:2916–23.

23.   Sharma S V., Lee DY, Li B, Quinlan MP, Takahashi F, Maheswaran S, et al. A Chromatin-Mediated Reversible Drug-Tolerant State in Cancer Cell Subpopulations. Cell. Elsevier Ltd; 2010;141:69–80.

24.   Glasspool RM, Teodoridis JM, Brown R. Epigenetics as a mechanism driving polygenic clinical drug resistance. Br J Cancer. 2006;94:1087–92.

25.   Kurata T, Tamura K, Kaneda H, Nogami T, Uejima H, Asai G, Nakagawa K FM. Effect of re-treatment with gefitinib ("Iressa", ZD1839) after acquisition of resistance. Ann Oncol. 2004;15:173–177.

26.   Yano S, Nakataki E, Ohtsuka S, Inayama M, Tomimoto H, Edakuni N, Kakiuchi S, Nishikubo N, Muguruma H SS. Retreatment of lung adenocarcinoma patients with gefitinib who had experienced favorable results from their initial treatment with this selective epidermal growth factor receptor inhibitor: a report of three cases. Oncol Res. 2005;15:107–11.

27.   Shao DD, Xue W, Krall EB, Bhutkar A, Piccioni F, Wang X, et al. KRAS and YAP1 converge to regulate EMT and tumor survival. Cell. Elsevier; 2014;158:171–84.

28.   Premsrirut PK, Dow LE, Kim SY, Camiolo M, Malone CD, Miething C, et al. A rapid and scalable system for studying gene function in mice using conditional RNA interference. Cell. 2011;145:145–58.

29.   Barbie D a, Tamayo P, Boehm JS, Kim SY, Moody SE, Dunn IF, et al. Systematic RNA interference reveals that oncogenic KRAS-driven cancers require TBK1. Nature. 2009;462:108–12.

30.   Hyvarinen A, Oja E. Independent component analysis: algorithms and applications. Neural Networks. 2000;13:411–30.

31.   Rutledge DN, Jouan-Rimbaud Bouveresse D. Independent Components Analysis with the

JADE algorithm. Trends Anal Chem. Elsevier Ltd; 2013;50:22–32.

32. Subramanian A, Tamayo P, Mootha VK, Mukherjee S, Ebert BL. Gene set enrichment analysis : A knowledge-based approach for interpreting genome-wide. Proc Natl Acad Sci U S A. 2005;102:15545–15550.

33. Zhang Y, Wolf-yadlin A, Ross PL, Pappin DJ, Rush J, Lauffenburger DA, et al. Time-resolved mass spectrometry of tyrosine phosphorylation sites in the epidermal growth factor receptor signaling network reveals dynamic modules. Mol Cell Proteomics. 2005;4:1240–50.

34. Mertins P, Qiao JW, Patel J, Udeshi ND, Clauser KR, Mani DR, et al. Integrated proteomic analysis of post-translational modifications by serial enrichment. Nat Methods. 2013;10:634–7.

35. Bailey P, Chang DK, Nones K, Johns AL, Patch A, Gingras M, et al. Genomic analyses identify molecular subtypes of pancreatic cancer. Nature. 2016;531:47–52.

36. Wang MT, Holderfield M, Galeas J, Delrosario R, To MD, Balmain A, et al. K-Ras Promotes Tumorigenicity through Suppression of Non-canonical Wnt Signaling. Cell. 2015;163:1237–51.

37. Muzumdar MD, Chen P, Dorans KJ, Chung KM, Bhutkar A, Hong E, et al. Survival of pancreatic cancer cells lacking KRAS function. Nat Commun. 2017;1090:1–19.

38. Zhang Z, Wang Y, Vikis HG, Johnson L, Liu G, Li J, et al. Wildtype Kras2 can inhibit lung carcinogenesis in mice. Nat Genet. 2001;29:25–33.

39. Qian Z, Zhu G, Tang L, Wang M, Zhang L, Fu J, et al. Whole genome gene copy number profiling of gastric cancer identifies PAK1 and KRAS gene amplification as therapy targets. Genes Chromosom Cancer. 2014;53:883–94.

40. Cepero V, Sierra JR, Corso S, Ghiso E, Casorzo L, Perera T, et al. MET and KRAS gene amplification mediates acquired resistance to MET tyrosine kinase inhibitors. Cancer Res. 2010;70:7580–90.

41. Chen Y, McGee J, Chen X, Doman TN, Gong X, Zhang Y, et al. Identification of druggable cancer driver genes amplified across TCGA datasets. PLoS One. 2014;9.

42. Hofmann I, Weiss A, Elain G, Schwaederle M, Sterker D, Romanet V, et al. K-RAS Mutant Pancreatic Tumors Show Higher Sensitivity to MEK than to PI3K Inhibition In Vivo. PLoS One. 2012;7.

43. Mitra SK, Hanson DA, Schlaepfer DD. Focal adhesion kinase: in command and control of cell motility. Nat Rev Mol Cell Biol. 2005;6:56–68.

44. Kanteti R, Batra SK, Lennon FE SR. FAK and paxillin, two potential targets in pancreatic cancer. Oncotarget. 2016;7:31586–601.

45. McLean GW, Carragher NO, Avizienyte E, Evans J, Brunton VG FM. The role of focal-adhesion kinase in cancer - a new therapeutic opportunity. Nat Rev Cancer. 2005;5:505–15.

46. Sulzmaier FJ, Jean C, Schlaepfer DD. FAK in cancer: mechanistic findings and clinical applications. Nat Rev Cancer. 2014;14:598–610.

47. Zheng Y, Xia Y, Hawke D, Halle M, Tremblay ML, Gao X, et al. FAK Phosphorylation

40

by ERK Primes Ras-Induced Tyrosine Dephosphorylation of FAK Mediated by PIN1 and PTP-PEST. Mol Cell. 2009;35:11–25.

48. Hochwald SN, Nyberg C, Zheng M, Zheng D, Wood C, Massoll N a, et al. A novel small molecule inhibitor of FAK decreases growth of human pancreatic cancer. Cell Cycle. 2009;8:2435–43.

FIGURE LEGENDS

Figure 1: Sustained Kras knockdown in murine PDAC cells *in vitro*.

A. Schematic of lentiviral constructs used to express the reverse tetracycline transactivator (rtTA) and doxycycline-inducible shRNA system. P_{LTR} = 5'-Long Terminal Repeat promoter from MSCV backbone. P_{PGK} = mouse phosphoglycerate kinase promoter. Hygro = hygromycin resistance gene. P_{TRE} = tetracycline-response element minimal promoter. GFP = green fluorescent protein. Puro = puromycin resistance gene. GFP mRNA and hairpins are on the same transcript.

B. *Kras* mRNA levels following short-term (ST DOX, 4 days) or long-term (LT DOX, 21 days) DOX treatment of shLuc- or shKras-transduced cells. Gene expression is normalized to untreated condition with TATA binding protein (TBP) control. Average normalized *Kras* expression +/- 95% confidence intervals (n=3) of three independent clones from D parental cell line, using two independent hairpins and shLuc as control, is shown.

C. Western blot showed sustained Kras protein knockdown following LT DOX treatment.

D. Cell viability following ST (5 days) Kras knockdown normalized to untreated (No DOX) condition. Average cell viability +/- s.d. (n=4) is shown. *** $p<0.001$, two-tailed student t-test.

E. Phase-contrast images reveal morphological changes associated with ST and LT DOX treatment.

F. Growth curves of untreated (No DOX) and LT DOX cells transduced with shKras or shLuc. Average cell viability (normalized to day 0) +/- s.d. (n=4) is plotted.

Figure 2: The Kras-inhibited state is adaptive and reversible.

42

A. Clonal efficiency of Kras knockdown in four independent shKras clones (two from B line, two from D line, of which one harbors shKras.923 and the other harbors shKras.1442) based on the presence or absence of cells in wells plated with single cells. Clonal efficiency appeared parental line- but not clone- or hairpin-dependent. D line showed no difference in clonal efficiency in the presence or absence of DOX. B line showed a 25-35% decrease under DOX treatment. The majority of cells appeared to survive Kras knockdown. ****$p<0.0001$, chi-square test.

B. Quantitation of clone size 21 days after clonal expansion showed decreased clone size in LT DOX cells. Quantitation is based on solubilizaton of crystal violet stain and measurement of absorbance at 540 nm shown as box plots with 5-95% confidence. **** $p<0.0001$, two-tailed student's t-test with Welch correction for unequal variance.

C. *Kras* mRNA levels following DOX withdrawal (DOX WD) from LT DOX cells. Gene expression is normalized to untreated condition withTBP control. Average normalized *Kras* expression +/- 95% confidence intervals (n=3) of three independent clones from D line, using two independent Kras hairpins and shLuc as control, is shown.

D. Reversal of cell morphology following DOX WD. LT DOX images are same as **Fig. 1F**, as DOX WD cells are derived from LT DOX cells.

E. Reversal of proliferative rates by colony forming assay following DOX WD.

F. Re-induced sensitivity to Kras knockdown with DOX treatment in reverted cells. Cell viability following ST (5 days) Kras re-knockdown normalized to untreated (No DOX) condition. Average cell viability +/- s.d. (n=4) is shown. *** $p<0.001$, unpaired student t-test comparing to No DOX condition.

43

Figure 3: Characterization of tumor-initiating properties of Kras-inhibited PDAC cells.

A. Quantitation showing parental cell line variation in the efficiency of tumorsphere formation in matrigel-based 3D cultures with Kras knockdown. Average number of tumorspheres formed +/- s.d. (n=3) per 500 cells plated is shown.

B. Tumorspheres imaged 12 days after plating demonstrated decreased size in LT DOX.

C. Quantitation of tumor-initiating cell (TIC) number showed decreased TIC in LT DOX shKras-expressing cell lines.

D. Secondary cell lines derived from LT DOX-treated shKras-expressing tumors retained GFP expression. Phase-contrast and fluorescence images of representative secondary cell line at 18 days post-tumor dissociation (2nd LT DOX) are shown compared to the original cell line either untreated (No DOX) or treated with DOX for >21 days (LT DOX) *in vitro*.

E. *Kras* mRNA levels of pre-transplant and secondary cell lines derived from LT DOX-transplanted cells. Gene expression is normalized to untreated (No DOX) condition with TBP control. Average normalized *Kras* expression +/- 95% confidence intervals (n=3) is shown.

F. Western blot of cell lines in (E) demonstrated decreased Kras protein levels in secondary cell lines comparable to original cell line treated with DOX *in vitro* prior to transplant.

Figure 4: Gene expression analysis of Kras-inhibited cells shows minimal transcriptional changes.

A. Unsupervised hierarchical clustering across all expressed genes from RNA-sequencing data demonstrated segregation based on parental cell line and clone rather than Kras knockdown

44

status (red box = no DOX, uninhibited; green box = LT DOX, Kras-inhibited). Multiple

boxes of the same DOX condition for the same clone are replicates, which cluster together.

B. Heatmaps of DOX and Kras knockdown (KD) signatures derived from independent

component analysis of clone pairs in (A). Columns represent distinct gene expression

patterns (signatures), where colors encode directionality of gene expression and color

intensity denotes strength of signature (Z-score) for each sample.

C. DOX signature profile of individual cell line groups based on hairpin (shKras vs. shLuc) and

DOX treatment conditions. Higher scores indicate greater correlation of individual cell lines

with DOX signature. *p<0.05, Mann-Whitney U-test, comparing shKras/shLuc LT DOX vs.

shKras/shLuc No DOX.

D. Kras knockdown signature profile of individual cell line groups based on hairpin (shKras vs.

shLuc) and DOX treatment. Higher scores indicate greater correlation of individual cell lines

with DOX signature. *p<0.05, Mann-Whitney U-test, comparing shKras LT DOX vs. other

groups.

E. Network representation of overlapping enriched GSEA/MSigDB gene sets in the Kras

knockdown signature (p<0.05, FDR<0.25). Each circle represents a gene set with circle size

corresponding to gene set size and intensity corresponding to enrichment significance. Red

is upregulated and blue is downregulated. Each line corresponds to a minimum 50% mutual

overlap with line thickness corresponding to the degree of overlap. Cellular processes

associated with related gene sets are listed.

Figure 5: Unbiased phosphoproteomic analysis of signaling alterations in Kras-inhibited

cells.

A. Western blot of total phospho-tyrosine levels (total pY) showed increased total pY in Kras-
    inhibited cells. Blue arrows indicate protein bands exhibiting increased intensity in Kras-
    inhibited cells.

B. Overlap of pY peptides between 3 technical replicates of iTRAQ experiments. Criteria for
    such peptides are that they are unambiguously assigned, can be unique or not unique to a
    protein, phosphorylated, with an isolation interference ≤25 (low chance of contaminating or
    co-eluting peptides), and have a Mascot score of ≥25 (high confidence in the identification of
    the peptide).

C. Scatter plot of the ratio (LT DOX/No DOX) of the abundance of pY sites identified in at
    least 2 iTRAQ experiments. Focal adhesion-associated proteins containing upregulated pY
    sites in the LT DOX state in both B (B shKras.923 cl1) and D (D shKras.1442 cl2) lines are
    labeled (green). Changes in peptide abundance significantly correlated between the two
    subclones analyzed (p<0.0001, R^2 = 0.1875, Pearson correlation).

D. Scatter plot of the log2 ratio (LT DOX/No DOX) of the abundance of pY sites identified in
    SILAC. Focal adhesion-associated proteins containing upregulated pY sites in the LT DOX
    state in both B and D lines are labeled (green). Changes in peptide abundance did not
    significantly correlate between the two subclones (p=0.4601, R^2=0.004755, Pearson
    correlation).

Figure 6: Kras-inhibited cells exhibit enhanced adherence properties and dependence.

A. Immunofluorescence of vinculin revealed the distribution of focal adhesion plaques of No
    DOX and LT DOX cells. Scale bar indicates 20μm.

46

B. Quantitation of the percentage of cells containing focal adhesion plaques. Average % +/- s.d. (n=12) is shown. **** p<0.0001, two-tailed student's t-test, LT DOX vs. No DOX.

C. Quantitation of focal adhesions per cell area (μm^2). Average +/- s.d. (n=8) is shown. * p<0.05, Mann-Whitney U-test, LT DOX vs. No DOX.

D. Normalized cell number (LT DOX vs. No DOX) +/- s.d. (n=5) of adherent cells one hour after plating of single-cell suspension for shLuc and shKras-transduced clones derived from A and D lines. *** p<0.001, **** p<0.0001, two-tailed student's t-test, LT DOX vs. No DOX.

E. Phase-contrast images of Kras-uninhibited (No DOX) and -inhibited (LT DOX) clone pairs 1 hour after treatment with the actin polymerization inhibitor latrunculin B.

F. Western blot showed increased expression of the apoptotic marker cleaved-caspase 3 (CC3) in Kras-inhibited cells after forced suspension growth for 48 hours.

G. Normalized cell viability +/- s.e.m. (n=6) of cells grown in suspension with or without 2% matrigel. Brightfield and fluorescence images of LT DOX tumorspheres maintaining GFP expression are shown.

Figure 7: KRAS-inhibited 8988T cells exhibit altered cell proliferation and enhanced adherence properties and dependence.

A. *KRAS* mRNA levels for no DOX, DOX-treated (10 days), and WD DOX (DOX for 5 days, no DOX for 5 days) of shLACZ.1650- or shKRAS.407-transduced 8988T cells. Gene expression is normalized to untreated condition with beta-actin (ACTB) control. Average normalized *Kras* expression +/- s.e.m. (n=2) is shown.

B. Cell viability following ST (5 days) KRAS knockdown normalized to untreated (No DOX) condition for 8988T cells transduced with inducible shLACZ.1650 (iLACZ) or shKRAS.407 (iKRAS). WD: 8988T iKRAS-transduced cells treated with DOX for 5 days and then taken off DOX for 5 days restoring proliferation. WD cells exhibited reduced cell viability following repeat DOX treatment and KRAS knockdown. Average cell viability +/- s.d. (n=5) is shown. *** p<0.001, two-tailed student t-test comparing to No DOX condition).

C. KRAS knockdown decreases colony forming ability of 8988T cells, which is partially reversed (proportional to the increase in KRAS expression in (A)) following DOX withdrawal (WD).

D. Immunofluorescence of vinculin revealed the distribution of focal adhesion plaques of No DOX and LT DOX cells. Scale bar indicates 20μm.

E. Western blot showed increased expression of the apoptotic marker cleaved-PARP (cPARP) in KRAS-inhibited cells after forced suspension growth for 48 hours.

F. Quantitation of the percentage of cells containing focal adhesion plaques. Average % +/- s.d. (n=12) is shown. **** p<0.0001, two-tailed student's t-test for designated comparisons.

G. Quantitation of the number of focal adhesions per cell area (μm^2). Average +/- s.d. (n=8) is shown. ** p<0.01, **** p<0.0001, two-tailed t-test for designated comparisons.

48
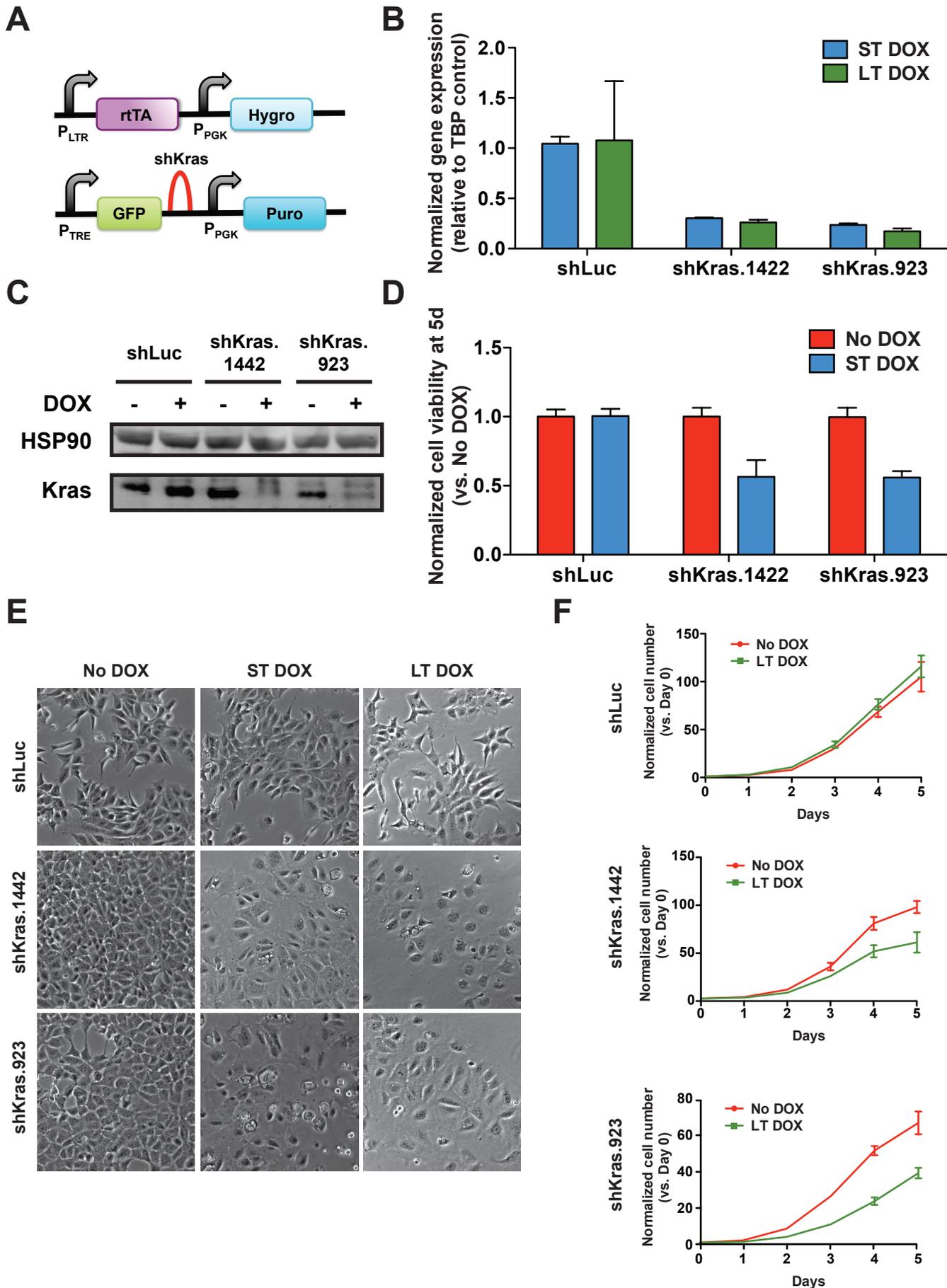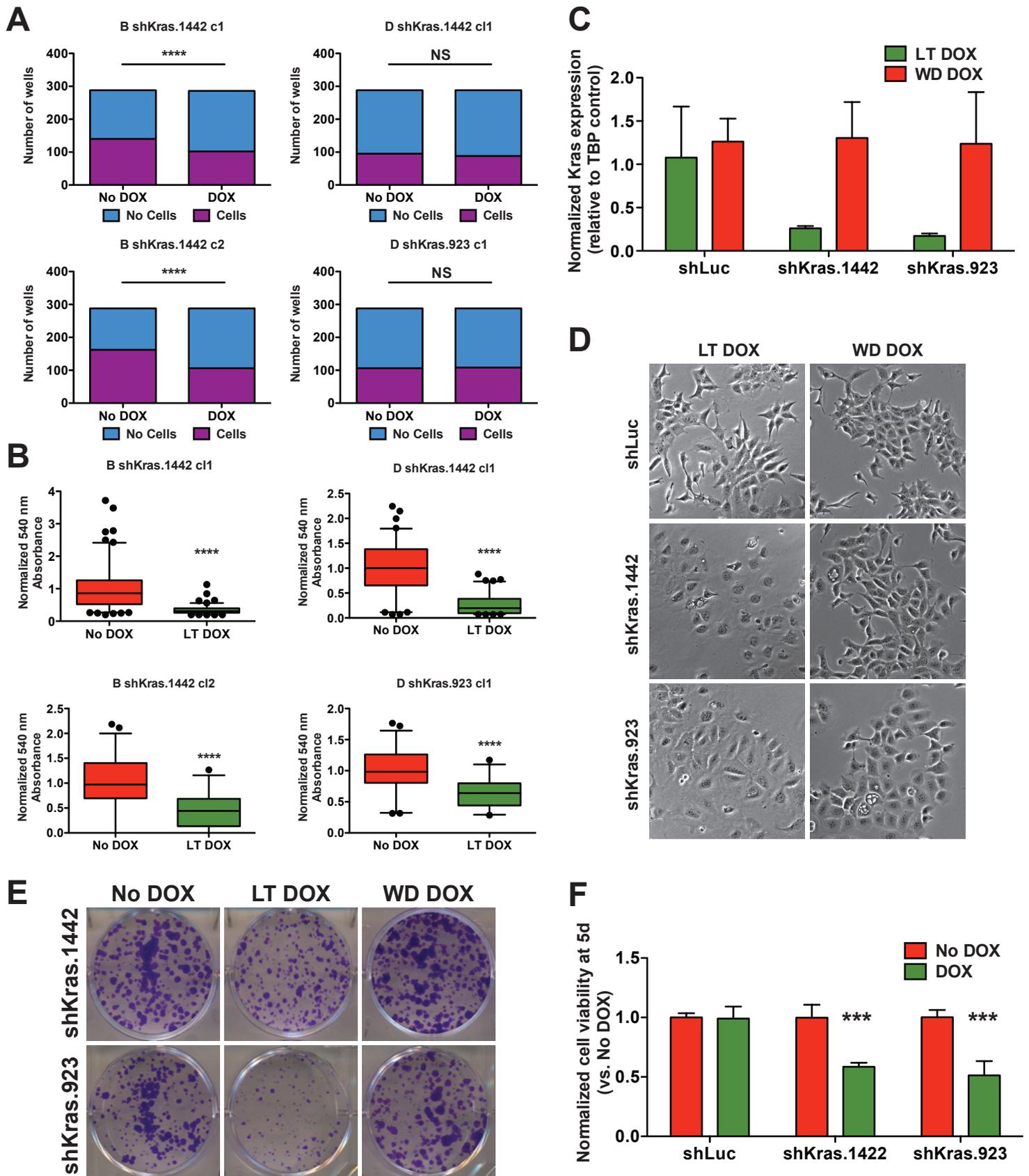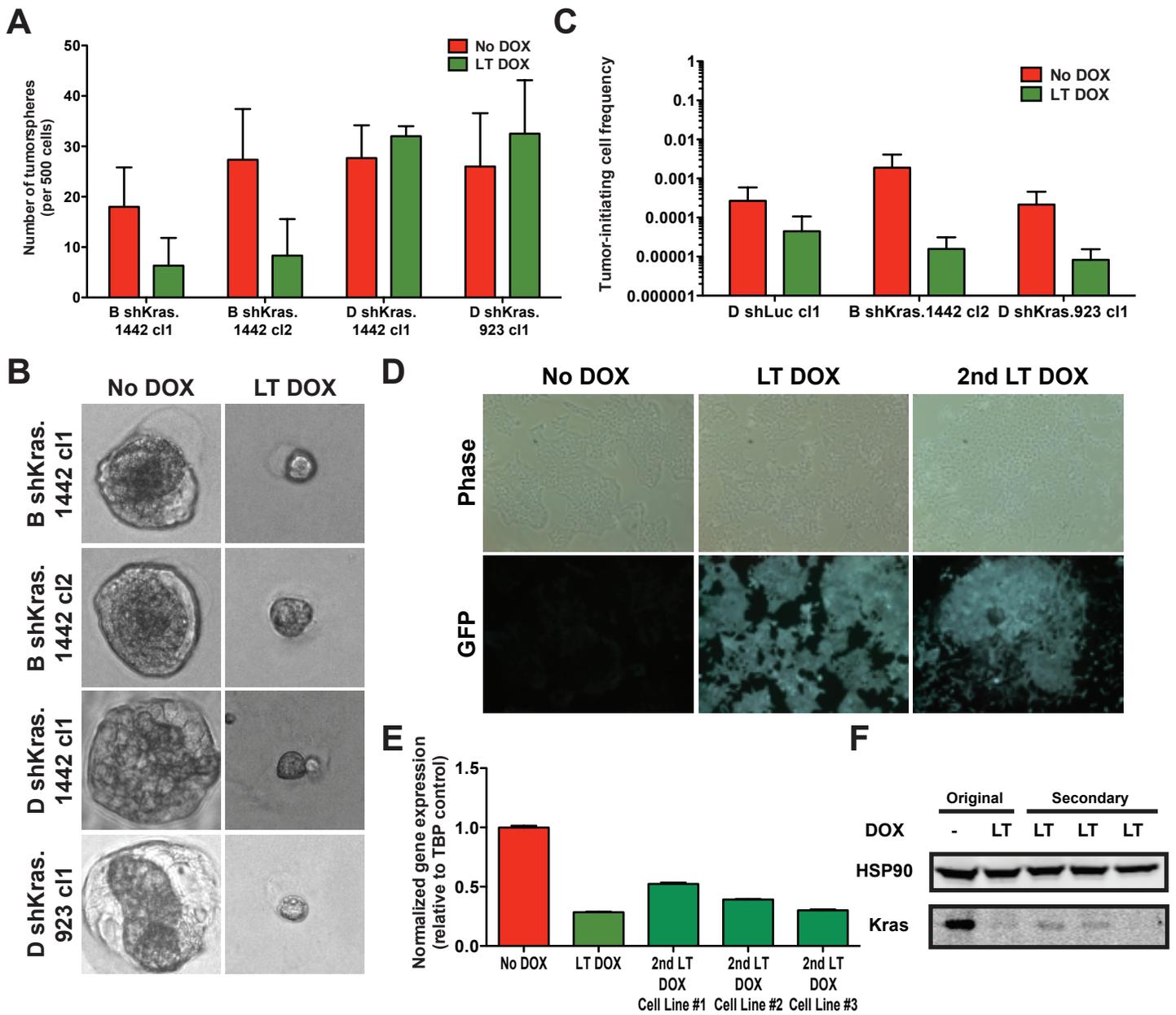
Figure 1

Figure 2

Figure 3
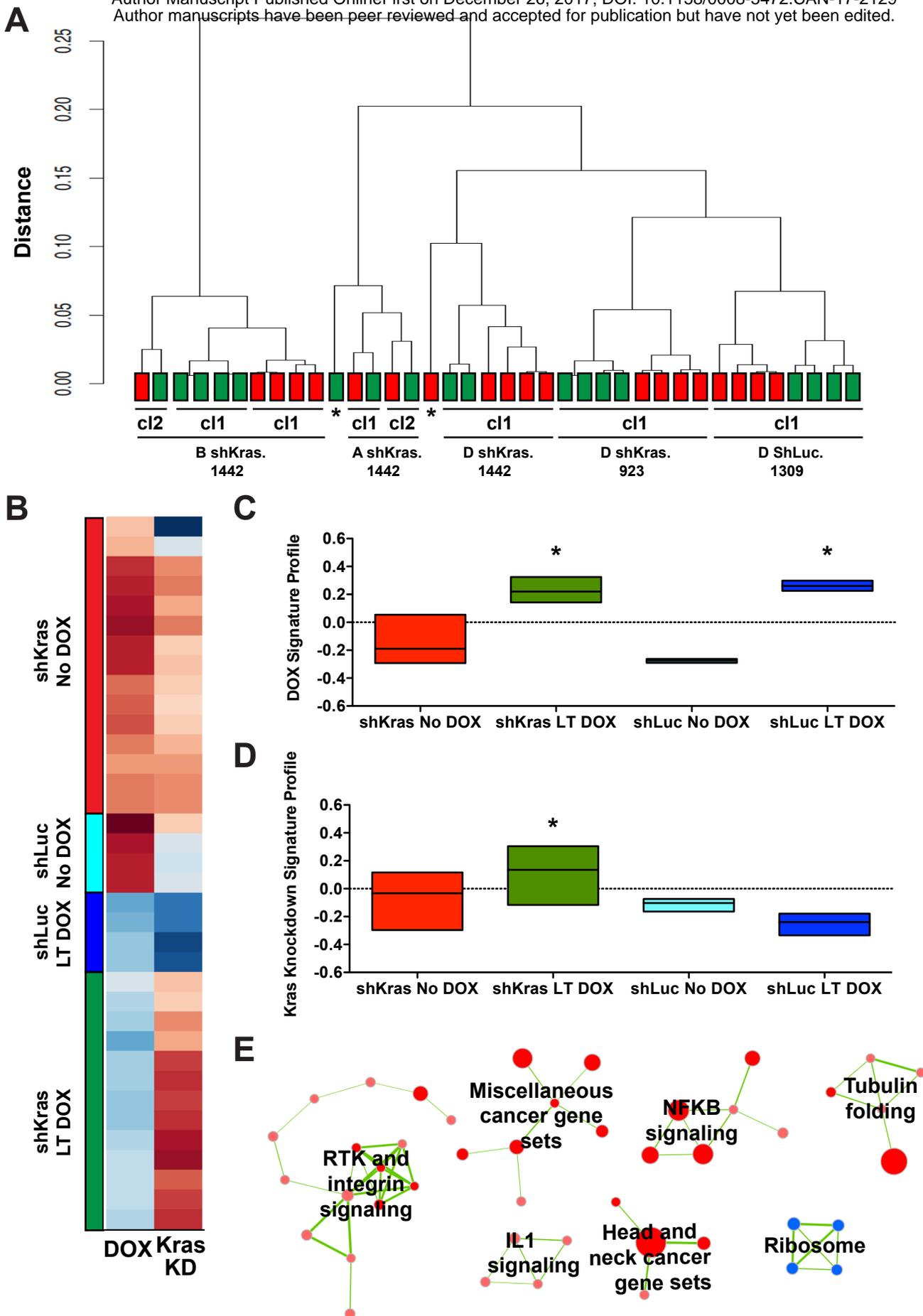
Figure 4
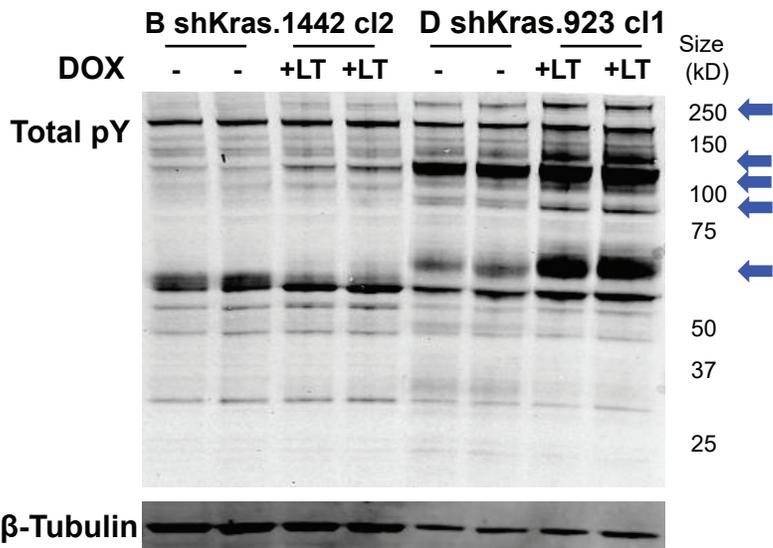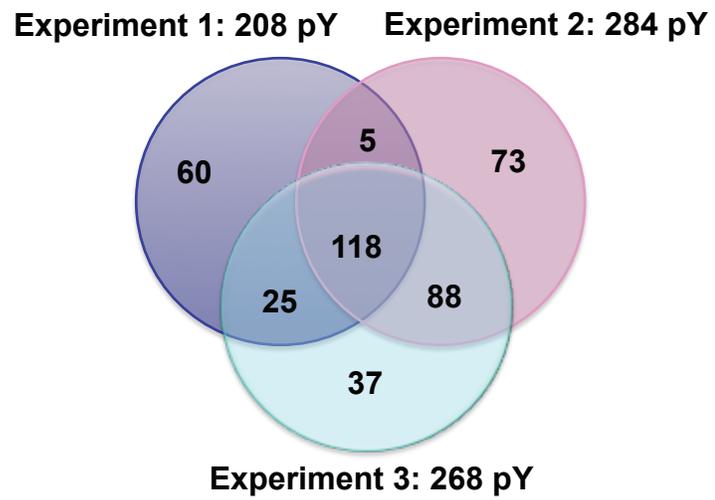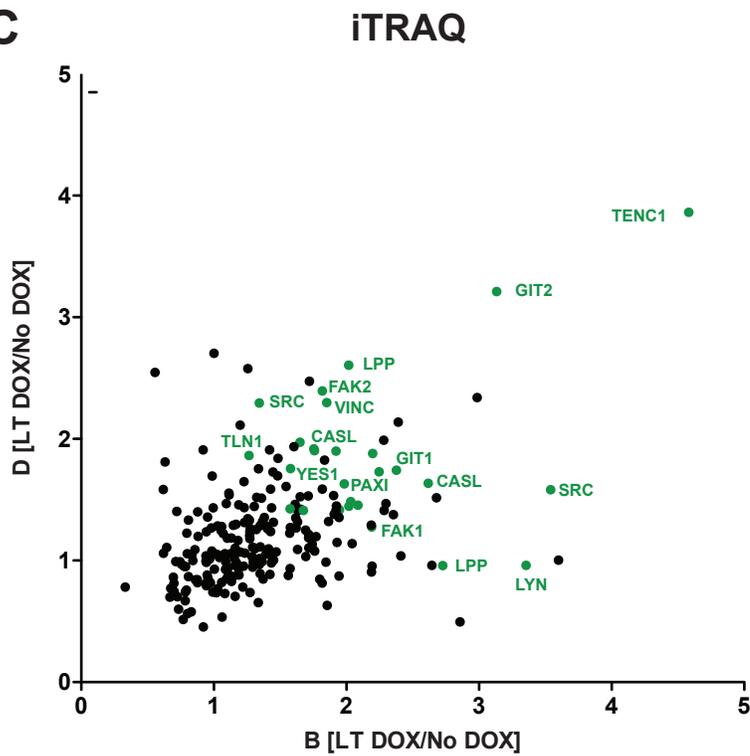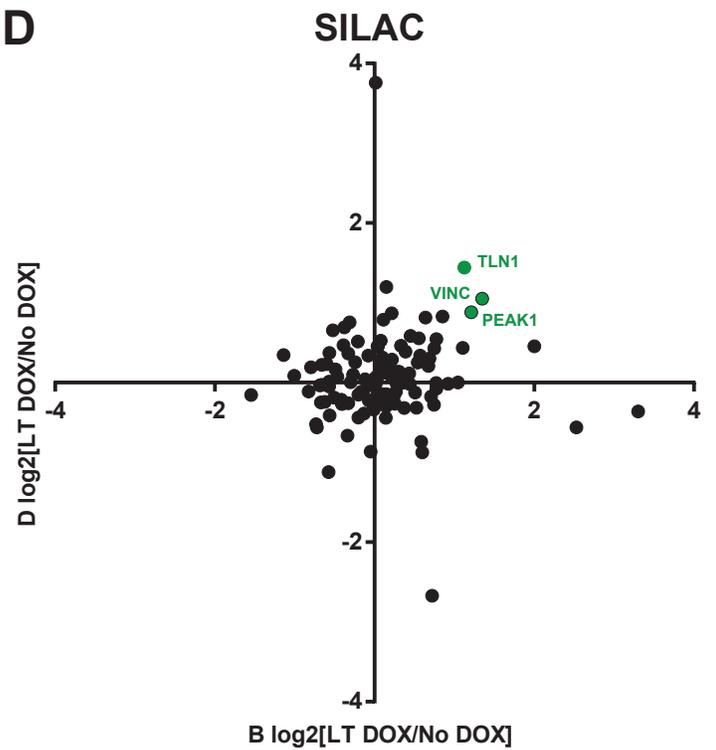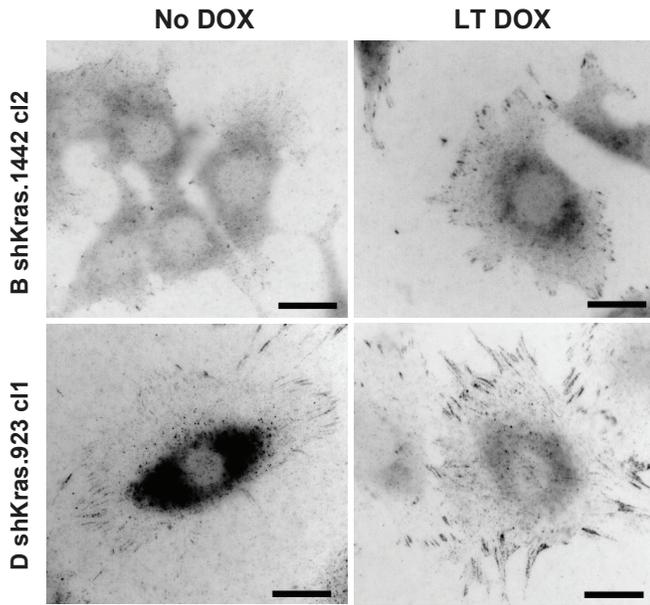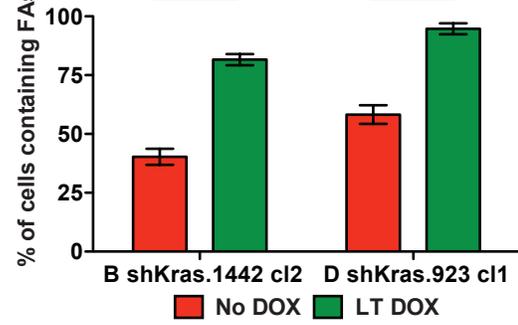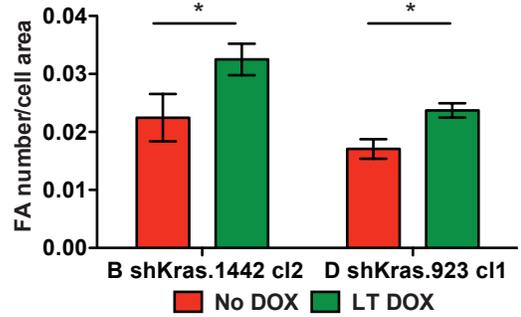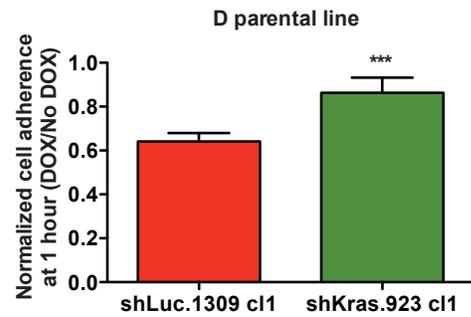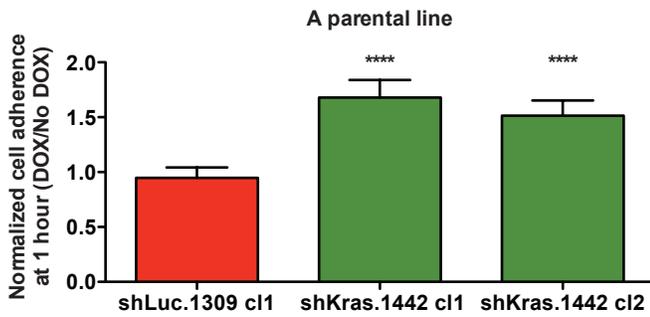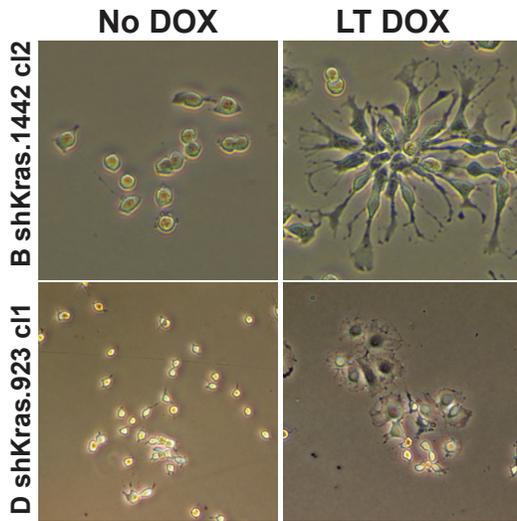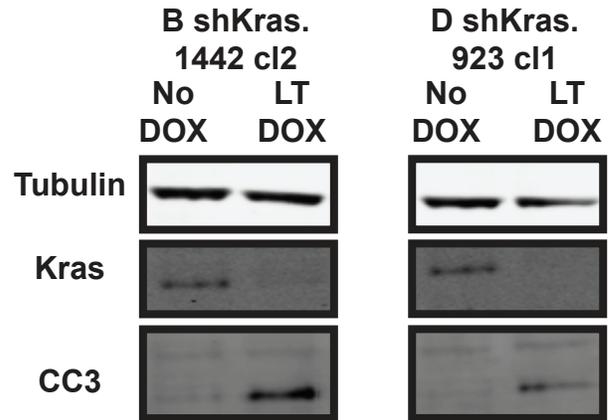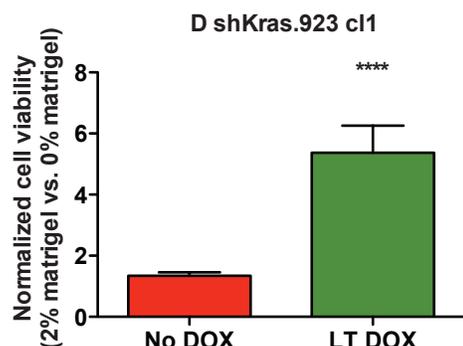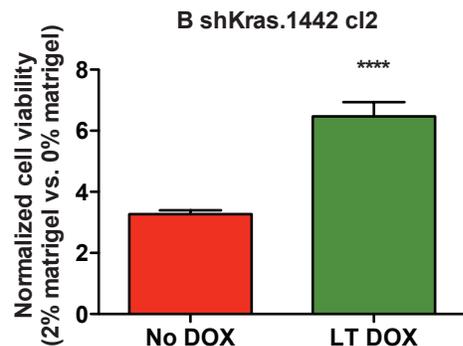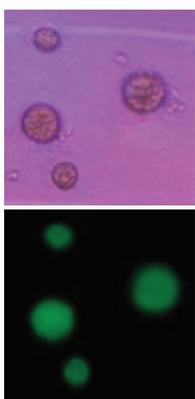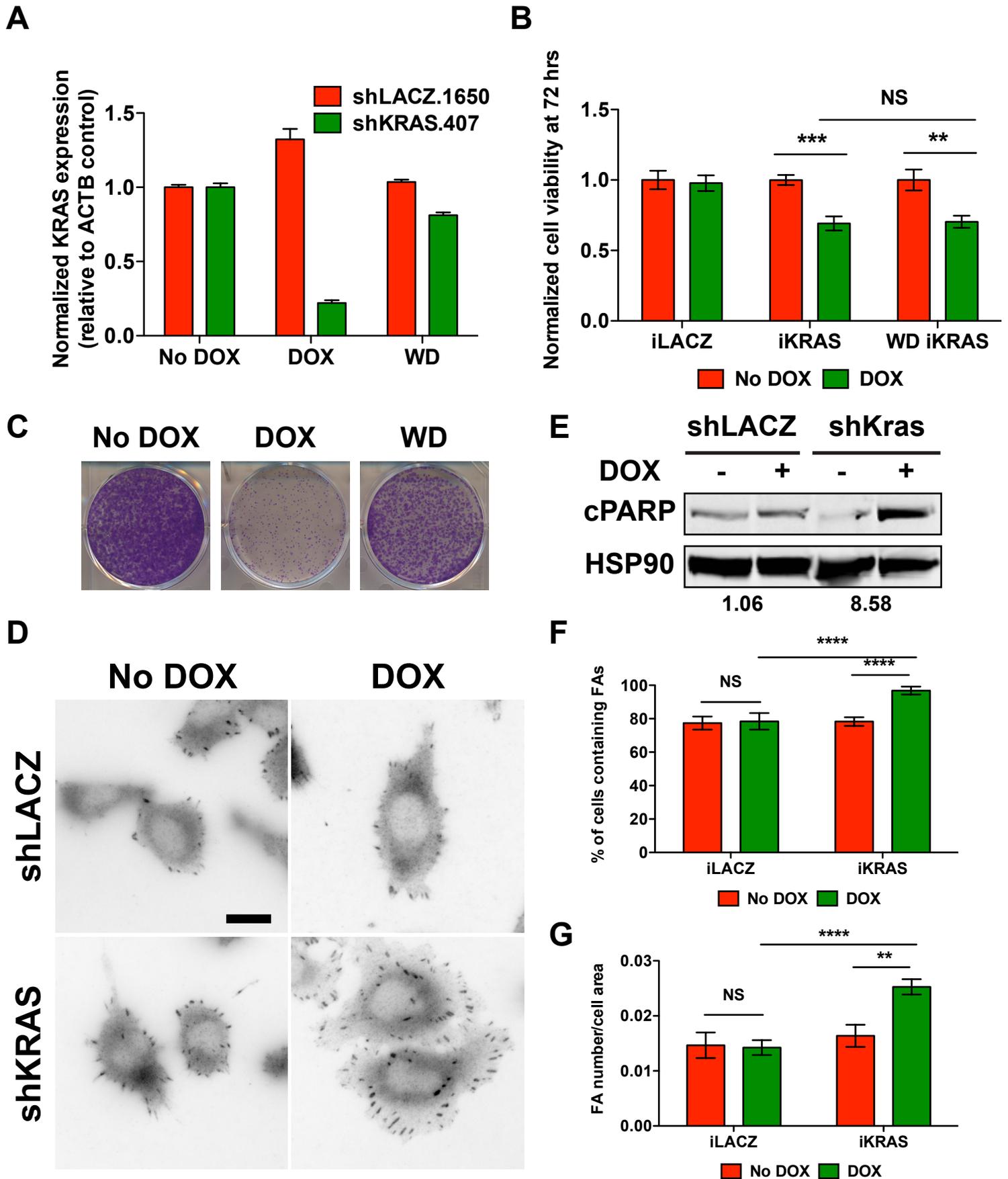
Figure 5

Figure 6

**Figure 7**

Cancer Research

The Journal of Cancer Research (1916–1930) | The American Journal of Cancer (1931–1940)

AACR American Association for Cancer Research

Adaptive and reversible resistance to Kras inhibition in pancreatic cancer cells

Pan-Yu Chen, Mandar D Muzumdar, Kimberly Judith Dorans, et al.

Cancer Res Published OnlineFirst December 26, 2017.

Updated version	Access the most recent version of this article at: doi:10.1158/0008-5472.CAN-17-2129
Supplementary Material	Access the most recent supplemental material at: http://cancerres.aacrjournals.org/content/suppl/2017/12/23/0008-5472.CAN-17-2129.DC1
Author Manuscript	Author manuscripts have been peer reviewed and accepted for publication but have not yet been edited.

E-mail alerts	Sign up to receive free email-alerts related to this article or journal.
Reprints and Subscriptions	To order reprints of this article or to subscribe to the journal, contact the AACR Publications Department at pubs@aacr.org.
Permissions	To request permission to re-use all or part of this article, use this link http://cancerres.aacrjournals.org/content/early/2017/12/23/0008-5472.CAN-17-2129. Click on "Request Permissions" which will take you to the Copyright Clearance Center's (CCC) Rightslink site.